



# **Extending Capabilities of Mudrac Simulation Software**

Toluwalase Agoro

Institute of Mathematics, Physics and Computer  
Science

Aberystwyth University / Prifysgol

Engineering Physics (MEng)

3<sup>rd</sup> year dissertation

May 6<sup>th</sup>, 2022

# Table of Contents

Introduction .....	5
Literature Review.....	8
Introduction .....	8
Muons .....	8
History of Muons in matter.....	8
High energy slow-down .....	8
Low energy slow-down .....	9
Atomic capture.....	10
Cascade .....	10
Nuclear Capture .....	12
Muonic atom x-ray spectroscopy .....	12
Mudirac.....	15
Details of Mudirac.....	15
Performance and limitation of current software.....	17
Software extension .....	19
What software extension does .....	19
Software Structure.....	21
Experimental data from ISIS Neutron and Muon Source .....	26
Production of muons at ISIS.....	26
Experimental setup and method .....	27
Analysis of Data.....	28
Performance of software extension .....	31
Carbon.....	31
Silicon .....	32
Copper.....	32
Silver.....	33
Gold.....	33
Lead.....	34
Overview of bar charts.....	34
Use in elemental analysis.....	34
Discussion.....	36
Conclusion.....	37
Acknowledgements.....	37
Appendix A.....	38

Appendix B .....	41
Appendix C .....	42
Bibliography .....	43

## General Audience Summary

Muonic atom x-ray spectroscopy is a non-destructive method of determining what elements a sample is composed of. This method involves measuring the x-rays emitted from the interactions of the sample with a negative muon, which is a sub-atomic particle that can be thought of as a heavier analogue of the electron for this purpose. These emitted x-rays are not fully understood yet, so the purpose of this project is to calculate the intensities of the emitted x-ray by extending an already existing software package Mudirac, which currently gives the wavelength of emitted x-rays.

## Abstract

Muonic x-rays emitted from negative muons implanted in a sample can serve as a depth-dependent and non-destructive probe for elemental analysis, that is mainly used for cultural heritage materials. These x-rays are characteristic of elements present in the sample. While there are lists of these muonic x-rays and a software package Mudirac, dedicated to calculating the energies of muonic x-ray by solving the radial Dirac equation for a muon in an atom, these lists are incomplete as many are missing the intensities of these emitted x-rays. Therefore, this project aims to attempt to determine a dependable method of calculating the intensities of these muonic x-rays by extending and using outputs of current Mudirac software, using the python programming language. The focus of the project is on calculating the l-distribution, the initial population of muons at the time of capture according to angular momentum. This method was determined to be more accurate for elements of higher nuclear mass by comparing results with experimental data from ISIS Neutron and Muon source.

## Introduction

Muons are elementary particles which belong to the lepton family. They have a mass of about 207 times that of an electron and have a half-life of about 2.2 microseconds. Muons decay via the weak nuclear interaction. Positive muons decay into positrons and neutrinos. While negative muons decay into electrons and neutrinos.

When a negative muon interacts with matter it first undergoes a high energy slow-down phase, the frictional force acting on muon is determined by the elastic collision between muon and atoms, this phase determines the depth distribution of muon in a sample, this distribution depends on the momentum of muons and the elemental composition of the material.

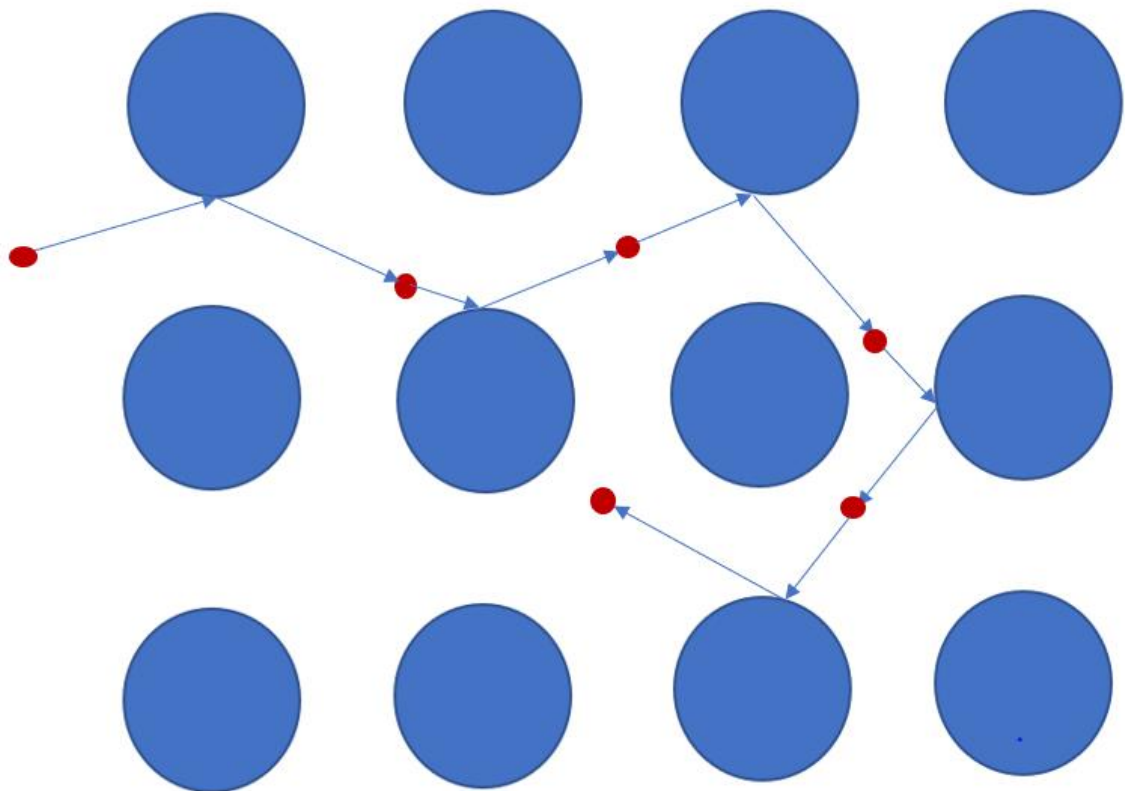


Figure1: Diagram illustrating how muons lose energy in high energy slow-down

Then comes the low energy slowdown in which the muons have energies comparable to those of the electrons in the atoms and the coulombic interactions with the electron cloud causes a frictional force to act on muons.

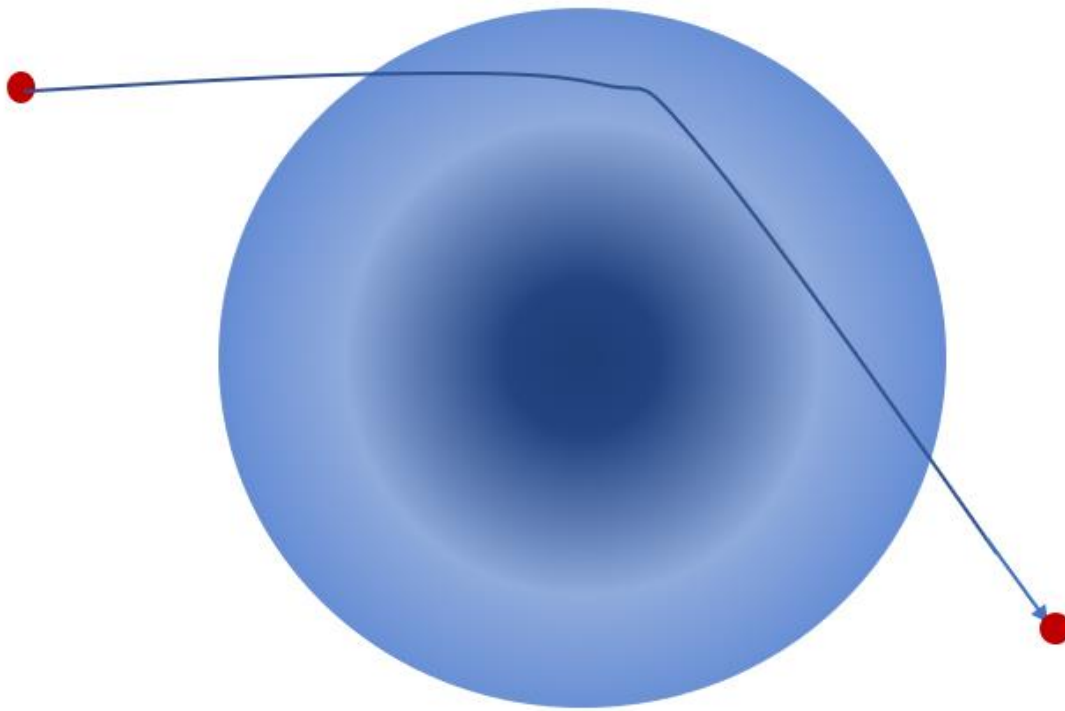


Figure 2: Diagram illustrating how muons interact with the electron cloud in low energy slow-down

The next phase, atomic capture is greatly affected by the low energy slow down, this determines the muon capture rates of atoms in chemical compounds and the initial population of muons in an energy shell according to the angular momentum known as the l-distribution when captured by atoms. Next is the muonic cascade, after the atomic capture, a muonic atom is formed, as the muon is captured at a high energy level it cascades down to the ground state emitting muonic x-rays. At the ground state, the muon may decay. Muons may also be captured by the nucleus of the atom; this causes the nucleus to become unstable and may transmute to an atom of a lower atomic number. The nucleus then emits gamma rays and or may emit several neutrons.

Muonic atom x-ray spectroscopy is a technique that utilizes negative muons and is mainly used as a non-destructive depth selective method to determine the elemental composition of a material. This technique exploits the muonic x-rays emitted during the muonic cascade, these x-rays are majorly dependent on the nuclear composition and to a lesser extent the electronic structure, and so they are characteristic of the elements present in the sample. The depth under investigation is determined by the momentum of muons, the maximum depth that can be reached varies from the elements present and phase of the sample this can be as large as a few meters in gases and a few centimeters in solid metals. This method is sensitive to almost all elements and has been shown to detect nuclei as light as lithium or as heavy as Lead and will work with any other nuclei heavier than lithium.

A major use of muonic atom x-ray spectroscopy is the elemental analysis of cultural heritage artefacts such as ancient roman coins, medieval swords, fragments of ancient statues,

sundials, and ancient pottery. Apart from elemental analysis, this technique has also been used for isotopic analysis, as slightly different nuclear structure causes slight shifts in energies of x-ray emitted which can be measured by high-resolution detectors.

Therefore, to utilize muonic atom x-ray spectroscopy as an effective technique it is important to understand the energies and intensities of x-rays emitted for each element. Although there is a comprehensive list of energies of muonic x-rays, there is little information on the intensities of emitted x-rays. While it is possible to determine the intensities experimentally, this is an expensive process as these experiments have to be done in large facilities which need a lot of resources to run and would be more cost-effective if these could be calculated and so a software package called Mudirac that solves the radial Dirac equation of the muon in an atom was created to determine the energy of x-rays and transition rates associated with x-rays was written to have a larger list of muonic x-rays, but this software does not have the capability to calculate the intensities of muonic x-rays. So, the purpose of this project is to extend the Mudirac software by using the output of the current software to calculate the intensities of x-rays.

# Literature Review

## Introduction

When a negative muon interacts with an atom it may be captured to form a muonic atom. This captured muon cascades from the initial higher energy level to the ground state, while cascading down it emits a series of muonic x-rays characteristic to atomic species [1]. Mudirac is a software package that solves the radial Dirac equation[2] for a muonic atom, and in doing so it calculates the energy of the muonic x-rays and transition rates relating to the muonic x-ray transitions [3]. The purpose of this project is to extend the Mudirac software to calculate the intensities of the muonic x-rays produced for pure elements using the outputs of current Mudirac software.

## Muons

Muons are leptons with a mass of  $1.88 \times 10^{-28}$  kg which is roughly 207 times the mass of an electron [4]. Unlike an electron which is stable, the muon has a half-life of about 2.2 microseconds [5] with that number varying depending on the material the muon is interacting with [6] and then decays into electrons or positrons with an assortment of neutrinos via the weak nuclear force depending on the type of muon involved [7].

$$\mu^- \rightarrow e^- + \bar{\nu}_e + \nu_\mu$$

$$\mu^+ \rightarrow e^+ + \bar{\nu}_\mu + \nu_e$$

This project will focus on negative muons and their interaction with the atom so any mention of muons from here will refer to negative muons unless specified.

## History of Muons in matter

The muon undergoes 5 major phases during the formation of a muonic atom as stated by Mukhopadhyay 1977, which are the high energy slow down, low energy slow-down, atomic capture, cascade, and nuclear capture [8].

### High energy slow-down

This stage is governed by Bethe- Bloch equation [9] [10] below which is the energy loss per unit path length traversed by a charged particle in matter:

$$\frac{dE}{ds} = \frac{4\pi e^4 N Z}{m v} \left[ \ln \left( \frac{2 m v^2}{I} \right) - \ln \left( 1 - \frac{v^2}{c^2} \right) - \frac{v^2}{c^2} - \frac{C}{Z} - \frac{\delta}{2} \right] \quad (1)$$

Where m and v are the mass and velocity of the muon, e is the elementary charge, Z is the atomic number of the target, C and  $\delta$  are correction terms, N is the density of atoms per unit volume, c is the speed of light and I is the mean excitation energy. This equation becomes less accurate without any corrections at lower energies as the charged particle may take some of the electron cloud with it [11] [12]. This phase will not be studied in-depth in this project as details of this phase does not greatly affect the next phase.



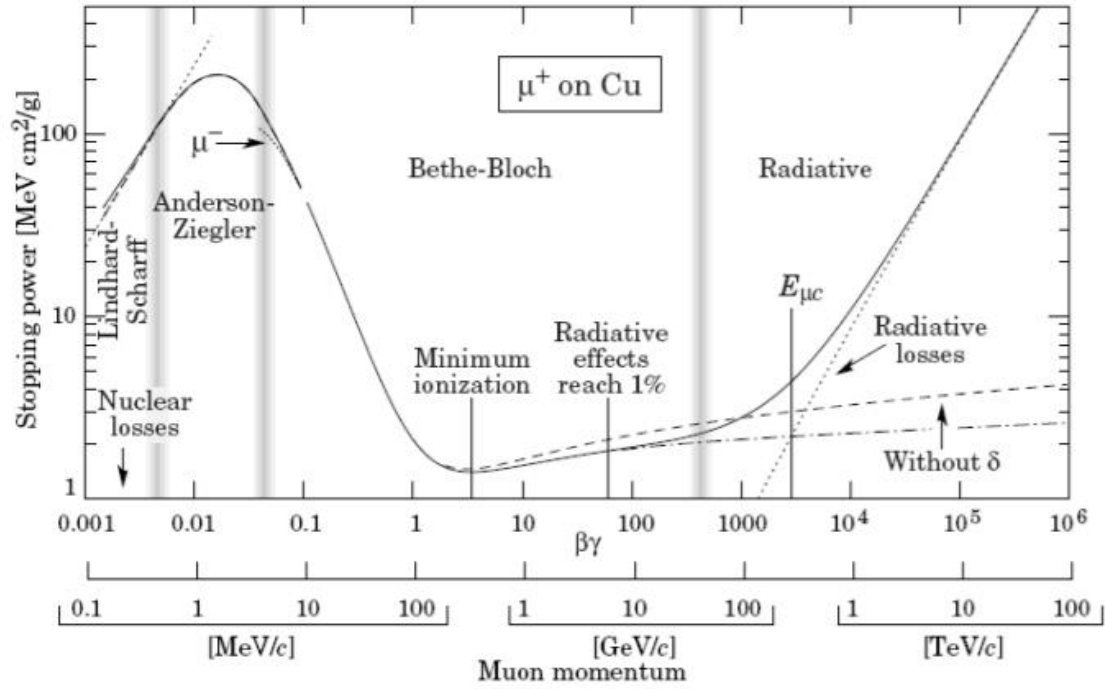


Figure 3: Graph showing stopping power of positive muon in copper as a function of the muon momentum, although the positive muon is not the muon of interest, the graph of the negative muon also follows a similar shape, this diagram also shows the regime within which Bethe-Bloch equation defines and the region that is defined to be the low energy slow-down phase. The energy loss per unit path length can be determined by multiplying the stopping power above by the density of copper in g/cm<sup>3</sup> [13].

### Low energy slow-down

At this phase, the muons have energies of about 2 KeV [14]. The equation describing this phase is the probability density distribution of energy transfer ( $\epsilon = \hbar\omega$ ) from the particle (in this case the muon) to the electron over time  $dt$  which is given below as equation 2 [15]. Where  $\epsilon^l$  is the Fourier transform of the longitudinal dielectric constant of the electron and is a function of  $k$  the wave vector and  $\omega$  the frequency the  $Im$  refers to the imaginary part,  $e$  is the elementary charge,  $\hbar$  is the reduced Planck's constant and  $v$  is the velocity of the muon as a function of time.

$$\frac{d^2p(\omega)}{d\omega dt} = \frac{e^2}{\pi\hbar v(t)} \int_{\omega}^{\infty} Im\left(\frac{1}{\epsilon^l(k, \omega)}\right) \frac{dk}{k} \quad (2)$$

Equation 2 can be used to create an equation that describes the frictional force that acts on the muon caused by the electron during this phase as was used by Haff et al [16] and is given directly below as equation 3.

$$\vec{F} = - \frac{4m_e^2 e^4}{3\pi\hbar^3} C(\chi) \vec{v} \quad (3)$$

$$C(\chi) = \frac{1}{2\left(1 + \frac{\chi^2}{3}\right)^2} \left[ \ln\left(\frac{1 + \frac{2\chi^2}{3}}{\chi^2}\right) - \frac{1 - \frac{\chi^2}{3}}{1 + \frac{2\chi^2}{3}} \right] \quad (4)$$

$$\chi^2 = \frac{m_e e^2}{\hbar^2 \sqrt[3]{3\pi^5 \rho(\vec{r})}} \quad (5)$$

The electron density  $\rho(r)$  and potential  $U(r)$  used by Haff et al was the Lenz- Jensen model[17]. Where  $m_e$  is the mass of an electron,  $e$  is the elementary charge,  $\hbar$  is the reduced Planck's constant and  $v$  is the velocity of the muon.

### Atomic capture

When a muon is captured by a compound, it is captured preferential by one atom rather than the other. These capture rates were first suggested by Fermi and Teller to be proportional to the atomic number of elements in species [14], but through experimental data, it was shown to need some corrections [18]. These atomic capture rates are not the objective of this project as most work will feature pure elements and the capture rates could be the objective of an entire project. The capture of the muon depends on the fact that the muon's energy loss is greater than kinetic energy minus the energy barrier in radial motion and not the average energy loss which is accurately described by equation 3 so it cannot be used to adequately describe the capture of the muon [19].

The important part of this phase relating to the intensities of muonic x-rays is the initial population of the muons in an energy level [20], which corresponds to the angular momentum distribution(l-distribution) of the muon at the time of capture can give population level of an energy level, different forms of l-distributions as well as initial energy level have been tried by Hartmann et al[21] and is given in appendix A. The initial energy level used by Hartmann et al was  $n = 20$  for some elements and  $n = 19$  for others [21] while Eisenberg and Kessler used a lower energy element of  $n=14$  which was also suggested by Eisenberg and Kessler that the l-distribution are relatively constant across all higher energy levels [22]. The l-distribution used by Vogel which is shown in appendix B has an energy level dependence and has a quadratic dependence in angular momentum [23].

The shape of l-distribution has been shown to be preserved at higher energy levels [24] which would allow these forms to be calculated if the rates at which these states are being filled are known. These l-distributions can also be calculated via several integro-differential equations which are shown in Appendix B and utilize equation 2.

### Cascade

The phase can be split into 2 stages: the classical stage and the quantal stage. The first part of this stage is treated classically as the quantum number are large and energies are small, so energy losses are treated in the same way in the low energy slow down using equation 3, the muon's path can be followed until it reaches the quantal phase[25], a portion of the trace of these orbits is shown in figure 2. At higher energy levels the changes in the muon's angular momentum are small so l-distribution is relatively unchanged, therefore the classical stage of this phase will not be of much interest in calculating the intensities of muonic x-rays[26].

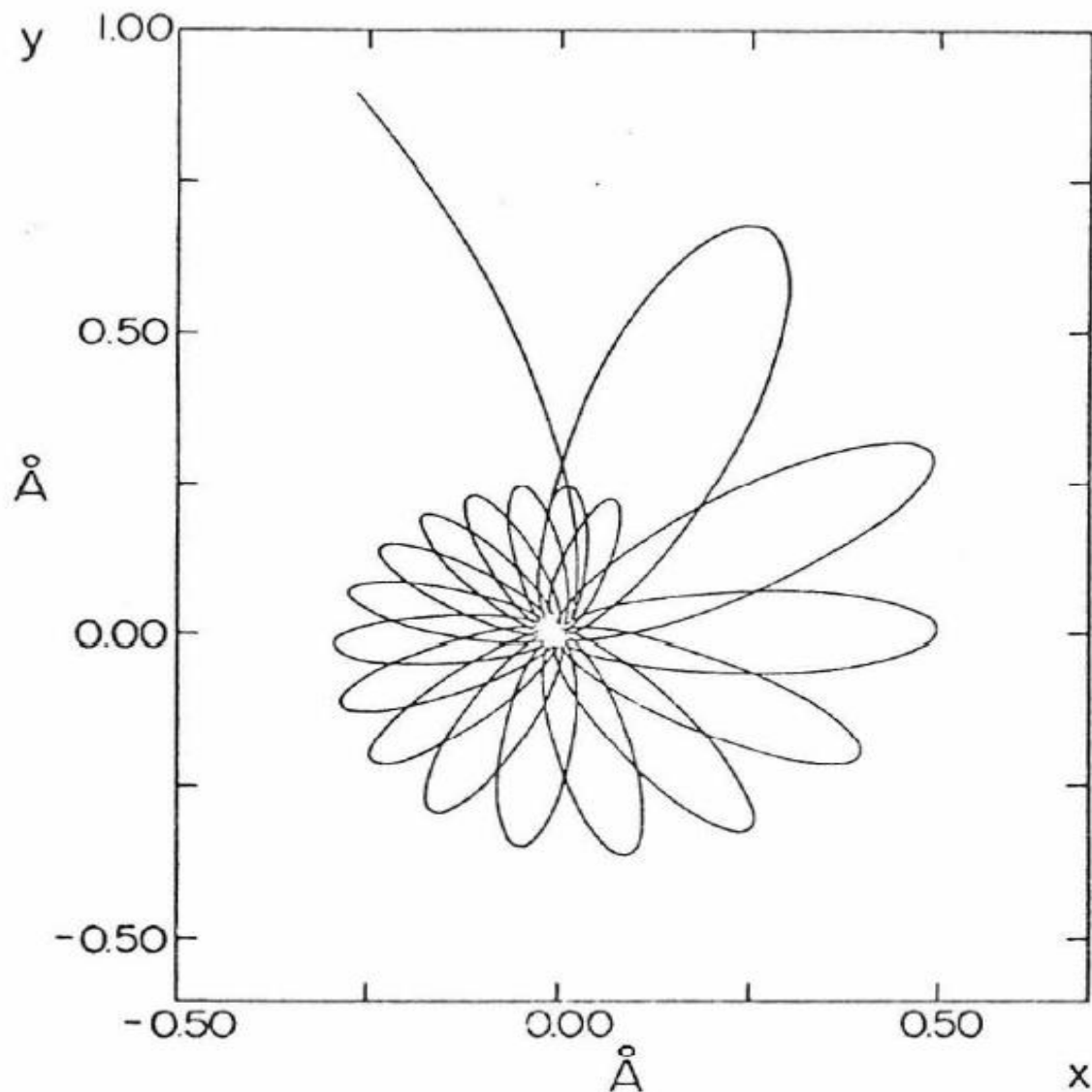


Figure 4: Trace of muon path when captured during the classical phase of cascade[26].

At the quantal stage, the muons can be well defined by energy levels [27] so transitions from these higher muonic energy levels to lower muonic energy levels emitting the muonic x-rays [28] of interest as is illustrated in figure 3 below. If the I-distribution at the start of the quantal phase is well-defined one can use the transition rates determined by Mudirac to calculate the intensities of muonic x-rays[29].

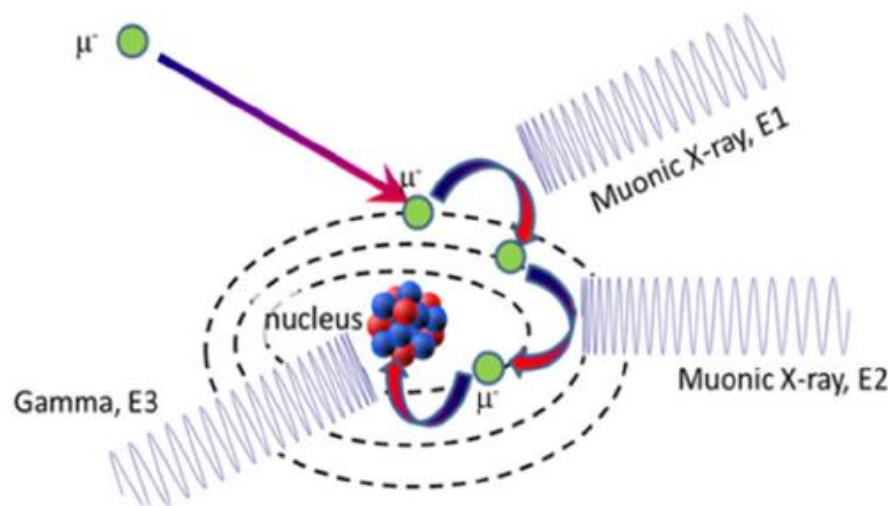


Figure 5: Diagram illustrating the muonic transitions and emitted x-rays[30].

### Nuclear Capture

When the muon reaches the lowest muonic energy state (1s), the muon may be captured at different rates [31] [32] by different nuclei which may cause a nucleus to transmute to another nucleus of lower Atomic number [33], and cause the unstable nuclei to emit gamma rays and may emit several neutrons [34].

The phases of major interest in this project are the atomic capture and cascade, as the I-distribution is majorly determined in atomic capture which is then used to calculate the intensities of x-rays emitted in cascade.

### Muonic atom x-ray spectroscopy

There are many techniques used to determine the elemental composition of a sample such as: nuclear activation analysis [35], laser ablation [36], nuclear magnetic resonance [37] and XRF (X-ray fluorescence) [38]. But many techniques are not non-destructive, depth-dependent as well as have a broad range of sensitivity such as muonic atom x-ray spectroscopy [39]. This technique involves irradiating a sample of interest with negative muons and measuring x-rays emitted in the cascade phase[40] and so it is important to understand the intensities of these muonic x-rays and is the driving force of this project.

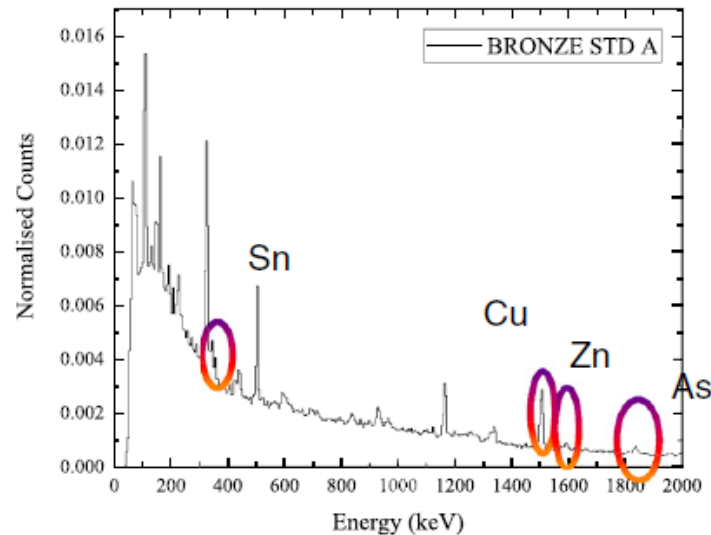


Figure 6: Muonic x-ray spectra of a bronze standard measured at ISIS Neutron and Muon source with peaks corresponding to the elements of interest labelled[40].

The depth under investigation is determined using equation 1 defined in the high energy slow down phase of muon and can be calculated using software like SRIM [41]. One of the powerful capabilities of this technique is its ability to detect light elements [42] such as lithium [43], which cannot be easily detected by many other methods. This technique is mainly used for cultural heritage artefacts which must not be destroyed by the method of investigation [44] such as ancient roman coins [30] [45] and bronze ship fragments [46], but has also been used to characterize other non-archaeological samples such as Carbonaceous chondrites [47], piezoelectric materials [48] and even organic materials like tissue samples[42]. This technique is not only used to characterize the elemental composition of samples but it has also been used for isotopic analysis as different isotopes have slightly different muonic x-rays [49].

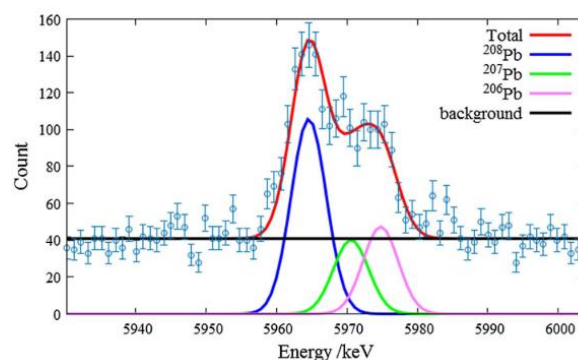


Figure 7: Graph showing the lead isotopic contribution to muonic x-ray peak[49].

This method also has some potential in determining the chemical environment of the sample as different chemical environments may cause slight deviations in x-ray intensities [50]. This technique has also been shown to have the capability of imaging where different elements are present in a sample and also producing a 3-d image of structure [51]. Gamma

rays from the nuclear capture phase after the cascade phase have also been shown to be a good probe for determining isotopes and even elements [52].

# Mudirac

## Details of Mudirac

The original Mudirac software was written in C++, which can be run on any Linux system without any dependencies and can be downloaded from the GitHub repository (<https://github.com/muon-spectroscopy-computational-project/mudirac>). This software takes in an input file with parameters for software to work with, such as nuclear composition, electronic composition, and transitions to calculate etc. A full list of parameters can be found in the Mudirac paper [3]. The software gives a text output file which gives the x-ray transition in IUPAC notation for x-ray spectroscopy [53], the energy of transition and the rate associated with the transition. An image of a text file is given below.

```
# Z = 79, A = 197 amu, m = 206.768 au
Line      DeltaE (eV) W_12 (s^-1)
K1-L2     5.55973e+06 1.60292e+18
K1-L3     5.72672e+06 1.74645e+18
K1-M2     8.03462e+06 2.36522e+17
K1-M3     8.07791e+06 2.97762e+17
K1-N2     8.9018e+06 8.10159e+16
K1-N3     8.91919e+06 1.06235e+17
K1-O2     9.2497e+06 1.43163e+16
K1-O3     9.27893e+06 4.33588e+16
K1-P2     9.4831e+06 7.36027e+15
K1-P3     9.4999e+06 2.37469e+16
K1-Q2     9.6223e+06 4.30738e+15
K1-Q3     9.63282e+06 1.4457e+16
K1-R2     9.71188e+06 2.74811e+15
K1-R3     9.71889e+06 9.4704e+15
K1-S2     9.77288e+06 1.86498e+15
K1-S3     9.77778e+06 6.54766e+15
K1-T2     9.81627e+06 1.32581e+15
K1-T3     9.81983e+06 4.71867e+15
K1-U2     9.84822e+06 9.77304e+14
```

Figure 8: Example of an output file from current Mudirac software.

The radial Dirac equation can be reduced to 2 coupled ordinary differential equations shown below [54]:

$$\frac{dG}{dr} = \frac{k}{r}G + \left(mc - \frac{E-V(r)}{c}\right)H \quad (6)$$

$$\frac{dH}{dr} = -\frac{k}{r}H + \left(mc + \frac{E-V(r)}{c}\right)G \quad (7)$$

Where the mass  $m$  used is the reduced mass of the system,  $V(r)$  is the potential muon experiences,  $c$  is the speed of light,  $k$  is a quantum number that can either be positive or negative but not zero, and can be gotten from angular momentum number  $l$ .

$$k = \begin{cases} -(l+1) \\ l \end{cases} \quad (8)$$

$G$  and  $H$  are parts of the wavefunction, where  $H$  is the component that is dominant at low energies and  $G$  is dominant at relativistic energies. The full wavefunction is shown below:

$$\Psi(r) = \begin{bmatrix} \frac{iH(r)Y_{lm}}{r} \\ -\frac{G(r)Y_{lm}}{r} \end{bmatrix} \quad (9)$$

Where  $Y_{lm}$  are the spherical harmonics [55].

The potential used in the Dirac equation is the Coulombic potential with the option of treating the nucleus as a point charge or more realistic treating the nucleus as a sphere with a finite size, distribution of charges in the nucleus sphere can be modelled as a uniform distribution or Fermi 2-term charge distribution. There were 2 corrections to potential added by software, the first being the Uehling potential [56], which accounts for the fact that electromagnetic force acts through intermediate particles, the photon, as per quantum field theory. The Uehling corrections are very small at large distances but come into play at atomic distances. The expression for the Uehling potential for 2 electrons acting as point charge is given below:

$$V_u(r) = \frac{-e^2}{4\pi r} \left( 1 + \frac{e^2}{6\pi^2} \int_1^\infty e^{-2rm_e x} \frac{2x^2+1}{2x^4} \sqrt{x^2-1} dx \right) \quad (10)$$

The second correction to potential is one caused by the electrons in atoms acting on captured muon. This can be calculated by applying Gauss' law by solving the differential equation below given that the charge density  $\rho$  is known:

$$\frac{\partial}{\partial r} \left( r^2 \frac{\partial V_Q}{\partial r} \right) = 4\pi r^2 \rho(r) \quad (11)$$

The electronic charge density is calculated by using a combination of all electronic orbitals, the orbitals were determined using the method used by Tauscher et al [57] where the nuclear charge seen by the electron is partly shielded by muon and electrons in lower shells. All these electronic orbitals were combined to form the entire electronic background charge density.

After solving the Dirac equation for energy eigenstates of system  $\Psi$  this can be used to determine the energy of the states by applying Hamiltonian to the wavefunction. Using the wavefunction the rates of muonic transitions can also be determined using Fermi's golden rule shown below which gives the rate of transition from  $\Psi_1$  and  $\Psi_2$ :

$$r_{12} \propto \left| \int \Psi_2^* \hat{H} \Psi_1 d^3\vec{r} \right|^2 \quad (12)$$



Where  $\hat{H}$  is the perturbation Hamiltonian.

While Mudirac was written for captured muons it can be used to solve the radial Dirac equation for captured electrons depending on parameters given in the input file as the mass of the captured particle can be set. This was used to test the accuracy of software as there is more information on the transition rates of electrons.

## Performance and limitation of current software

A major component of this project was using the original Mudirac software to calculate the transition rates and energies of transition, and so the time performance of the software had to be better understood. The graph below shows the time complexity of the Mudirac software.

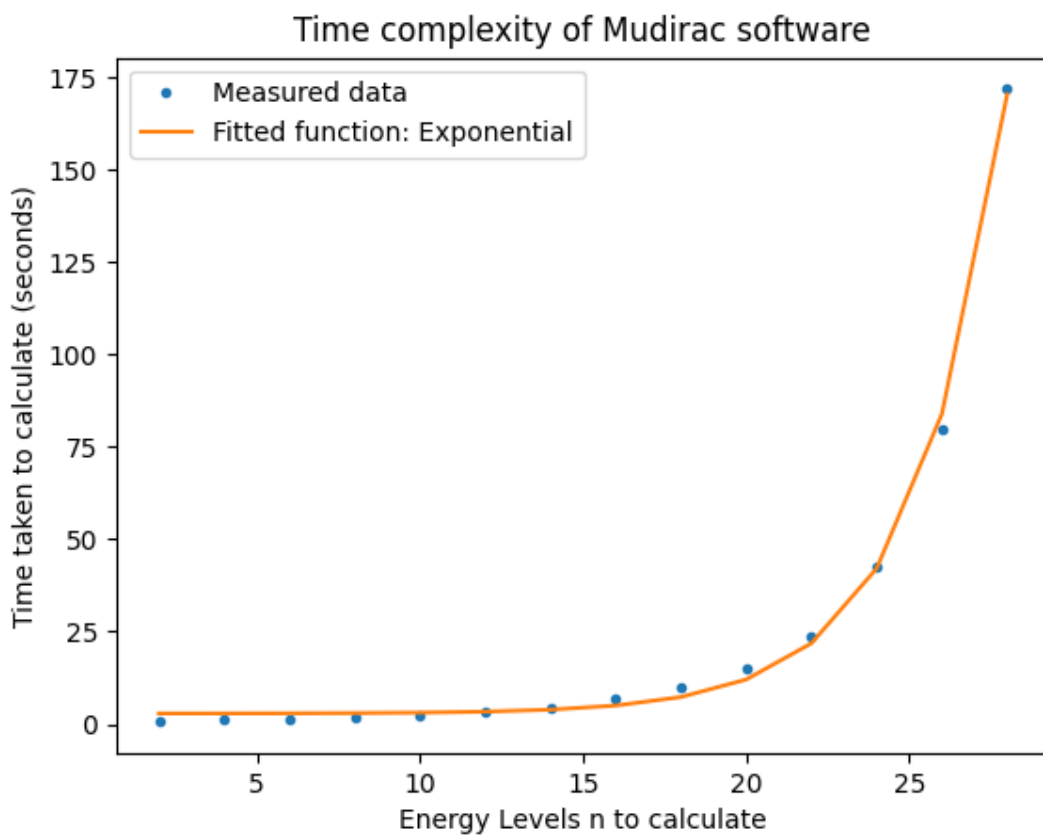


Figure 9: Graph showing how calculation times increase with energy levels being calculated and fitted function.

The graph above shows that the time complexity of the Mudirac software is exponential with energy level being calculated, using Big-O notation [58]  $O(e^{bn})$ , where  $b$  is equal to 0.3628 determined from fitting the measured data to function below:

$$f(x) = ae^{bx} + c \quad (13)$$

The fitted function can be used to extrapolate the time taken for higher energy levels, for  $n=40$  the time taken is 13027 seconds, just over 3 and a half hours, while for  $n=50$  the time taken is 489996 seconds, 5 days 16 hours. The exponentially increasing time caused calculations to be limited to  $n=40$ .

There were not any major differences in time taken when running Mudirac on more powerful systems, Mudirac was run on 3 computers:

- Personal Computer - Intel(R) Core(TM) i7-10510U CPU @ 1.80GHz with 12 GB of RAM
- Teaching Labs Computer - Intel(R) Core(TM) i7-4790T CPU @ 2.70GHz with 8 GB of RAM
- Shellsrv – The processor used on shellsrv is unknown but it has 24 CPUs with 128 GB of RAM

While fully testing the capabilities of software on these systems it was noticed that the first 2 systems could not reliably calculate energy levels higher than  $n=30$ . It is theorized to be caused by a lack of available space on RAM to calculate and could not be confirmed as there was no way to measure the space complexity. While the shellsrv could reliably run these calculations as it had enough RAM. As a result of this and the fact that the shellsrv could be left to run tasks for extended periods without timing out, the shellsrv proved to be the best choice to run Mudirac software. And so, the limiting factor in the calculation of energy levels is the time taken.

The original Mudirac software was limited from  $n=1$  to  $n=16$  as transitions and states to calculate are given in IUPAC x-ray spectroscopy notation and it is limited from K1 to Z31. So, the code had to be modified to allow even higher energy levels to be calculated. There was also a software bug which was discovered while using software which appeared when the input file was being read, this bug caused an error to be thrown and software to terminate when there is an empty line at the end of the input file. This bug was not fixed during the project as it was beyond the scope of the project and was just avoided for the length of the project.

# Software extension

## What software extension does

The major part missing in calculating the intensities of muonic x-rays is the I-distribution. The I-distribution can be calculated using the system of integro-differential equations given in appendix B. While this is the ideal method of determining the I-distribution, this method involves solving complex Integro-differential equations [59] and using DFT models of the electrons in the atom, so was deemed out of the scope of a 3<sup>rd</sup> year project. And so another method was employed which used the fact that I-distribution of muons was approximately preserved in higher energy levels as is shown in figure 31 in appendix B shown by Vogel et al[26]. This means that rates of transition are such that it roughly preserves I-distribution. While the I-distribution is not preserved exactly when cascading, a major approximation used by the software was that the I-distribution is preserved exactly from  $n = 40$  to  $n = 20$ . By using original Mudirac software to calculate all transitions between  $n = 40$  and  $n = 1$ , the rates computed were used to construct a transition matrix  $M$ , the steady-state population  $S$  of the matrix was determined and steady-state population over  $n=40$  and  $n=20$  was then fitted to one of the I-distribution forms given in appendix A, using the Levenburg-Marquadt[60] minimizer provided by Scipy and a least-squares cost function.

4 I-distribution forms were used, these were linear given by equation 18, constant given by equation 20, exponential given by equation 19 and quadratic given by equation 23. All shown in appendix A. The linear and constant forms do not require the steady-state to be calculated as they have no parameters to be fitted to the steady-state.

The steady-state was then found in an iterative method.

$$S_{i+1} = M(S_i + V) \quad (14)$$

With every iteration the lowest energy state was set to zero to avoid an accumulation of muons in this state, to simulate the nuclear capture effect at the lowest energy states, and equation 14 above was applied. Where  $V$  is a vector with only the topmost levels populated this is to ensure that there is a constant supply of muons into  $n=40$  energy level. The initial steady-state  $S_1$  is an empty vector. This was done until steady-state converged to a final value.

A graph of steady-state at  $n=20$  and fitted I-distribution form exponential is shown below.

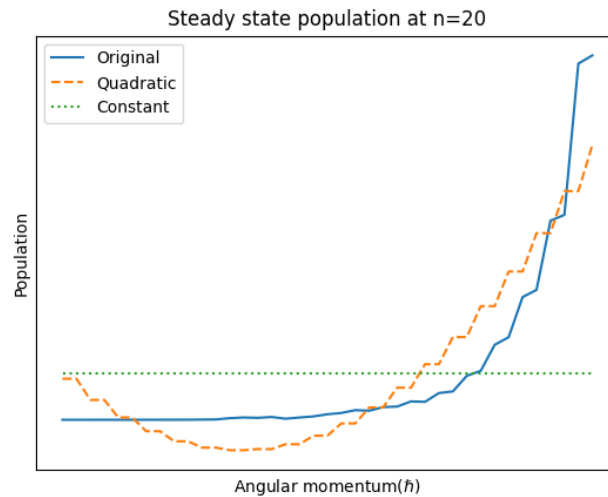


Figure 10: Graph of steady-state of gold at n=20 with quadratic and constant form of l-distribution

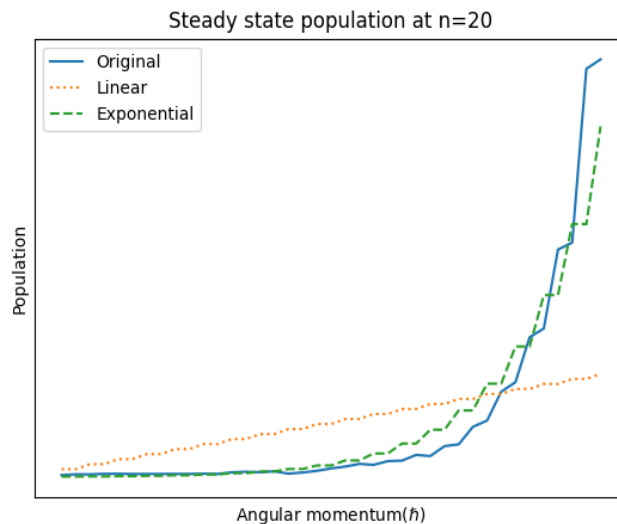


Figure 11: Graph of steady-state of gold at n=20 with exponential and linear form of l-distribution

With a known l-distribution, the next hurdle is determining which energy level  $n$  to start the x-ray emitting cascade. As l-distribution is thought to be preserved from  $n=40$  to  $n=20$ , the cascade was thought to be started from  $n=20$ . While there are x-rays emitted by transitions between  $n=40$  and  $n=20$ , these energies are too small to be measured experimentally as levels are close together in energies. With the starting energy level for cascade chosen, the determined l-distribution form was used to populate the starting energy levels  $n=20$ , these were then propagated down a probability tree, with the probability being determined by rates calculated by Mudirac software.

## Software Structure

The software extension was written in python [61] [62], as computation speed was not an issue, so quick development and easy access to software libraries were prioritized over computation time. Software is given in the GitHub repository ([https://github.com/tolu28-coder/Mudirac\\_extension](https://github.com/tolu28-coder/Mudirac_extension)). A separate Conda virtual environment with a dedicated python interpreter was created for this project to limit interference from other packages. The main python packages used for the project that are not part of built-in libraries are:

- NumPy: To have access to arrays, for dealing with large datasets and manipulating arrays.
- SciPy: For linear algebra tools, curve fitting and optimization.
- Scikit-learn: For creating neural networks.

The software was written in an object-oriented specific manner, with a class defined to achieve a specific purpose, then built up into larger classes, which uses the concept of composition, with larger top-level classes being composed of smaller classes, the structure of code is given below, which shows most of the defined classes and where they fit into code.

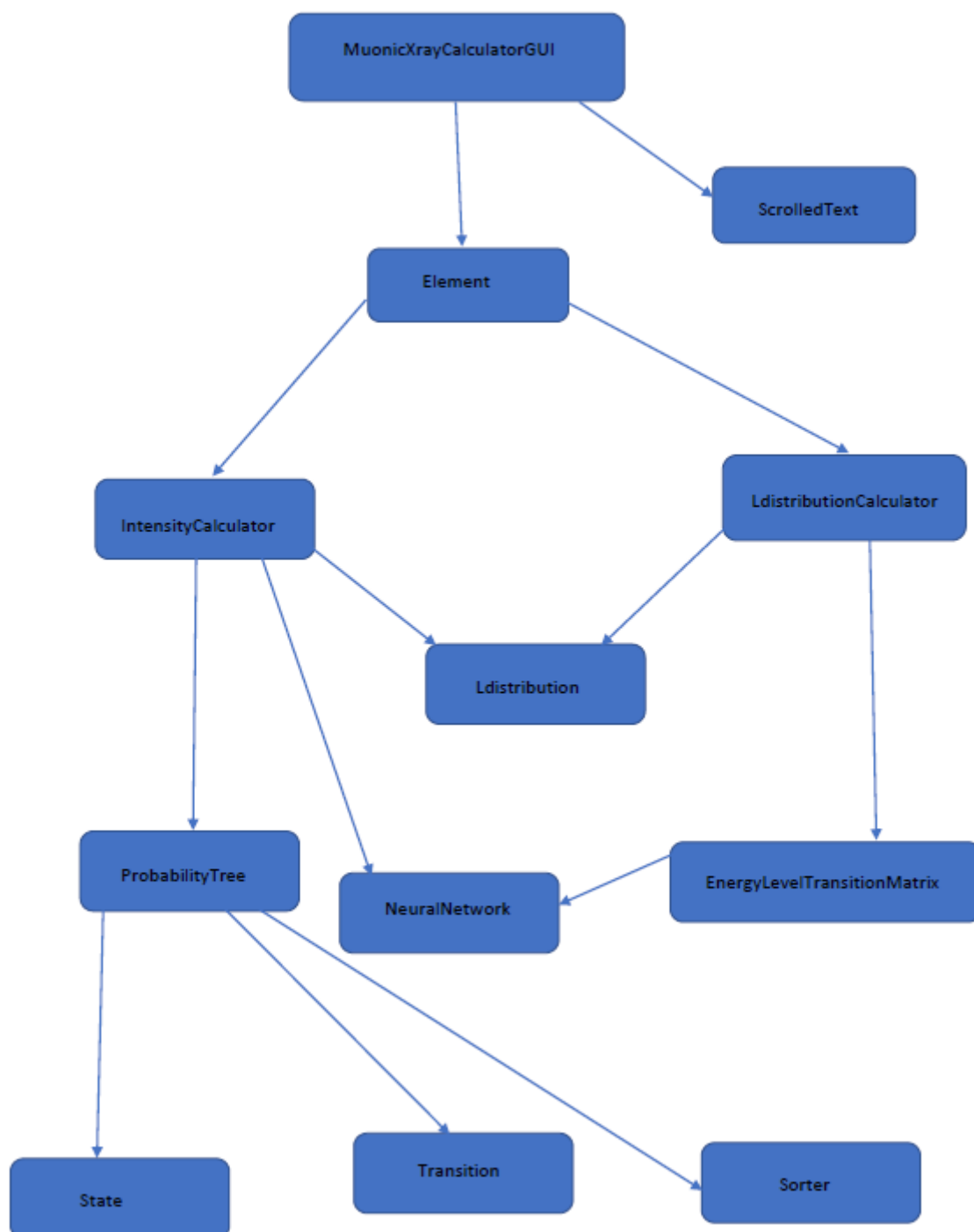


Figure 12: Diagram of class structure and how they relate to each other.

The top-level class, **MuonicXrayCalculatorGUI** is a GUI which allows users to use the extension given a Mudirac output file to use as an input file, without having to write a python script. An image of the GUI is given below as figure 13.

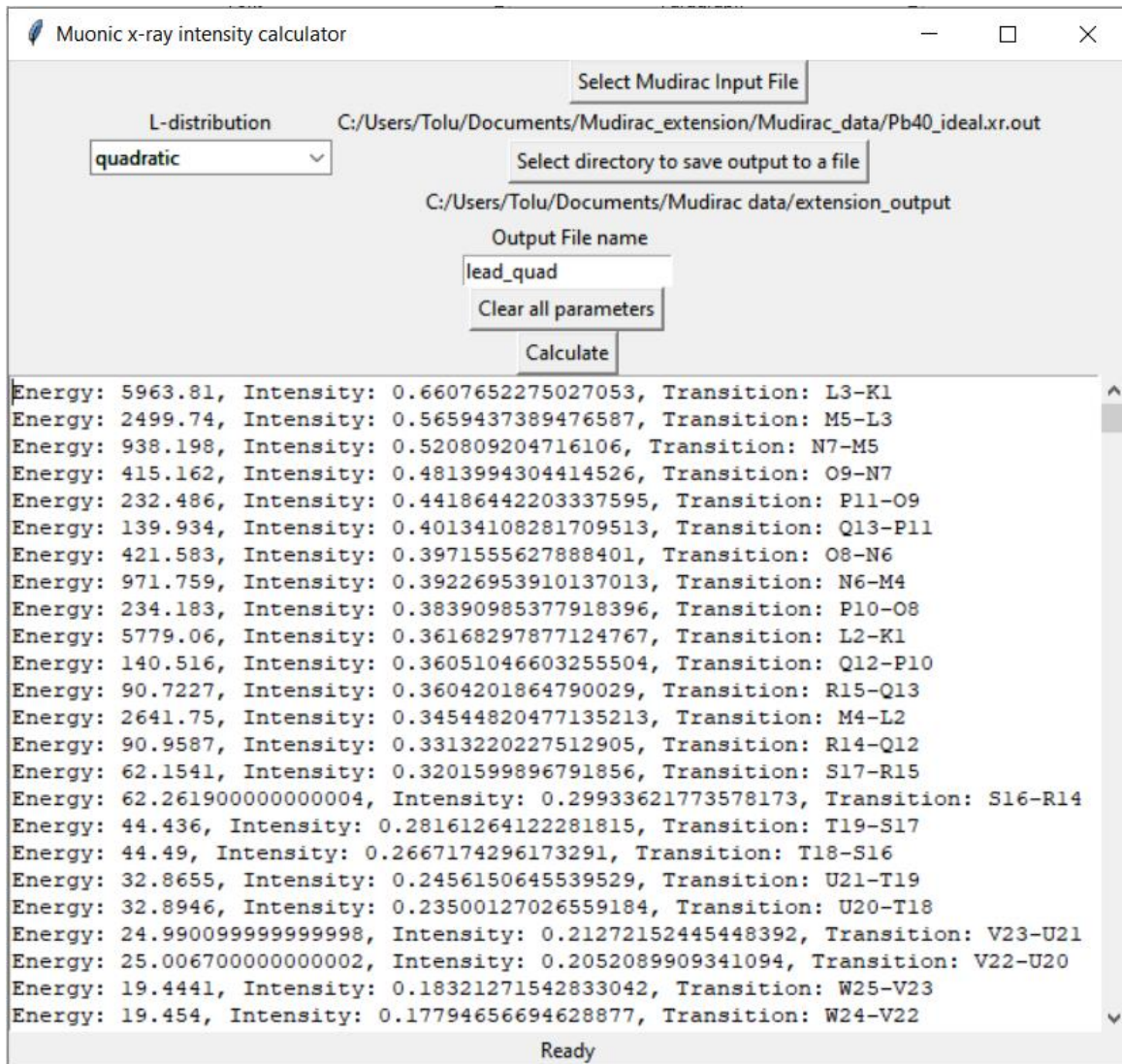


Figure 13: Image of final GUI

This object makes use of the Tkinter python library for GUI capabilities. This class is made of 2 defined subclasses **Element** and **ScrolledText**. The **ScrolledText** is a GUI widget which is used to display the Muonic x-ray intensities. This GUI makes use of a thread to run the **Element** class so as GUI will still be responsive to user input but will not start any new calculation while one is still ongoing.

The **Element** class calculates the intensities of X-rays given the output file. This **Element** class employs the **IntensityCalculator** and **LdistributionCalculator** classes. The **LdistributionCalculator** class calculates the L-distribution by employing the **EnergyLevelTransitionMatrix** class to calculate the steady-state population of muons given a path to an input file and the **Ldistribution** class to fit the steady-state population to one of the forms given in appendix A. The instance of the **Ldistribution** class that was fitted to steady-state population in **LdistributionCalculator** class and is then passed to the

**IntensityCalculator** class which uses this **Ldistribution** instance to calculate the l-distribution to use, the calculated l-distribution is used as an initial distribution for the **ProbabilityTree** class to calculate how many muons go through each transition and therefore the intensity. The **IntensityCalculator** class also parses the input file and passes the important transitions and energies to **ProbabilityTree** class. The **ProbabilityTree** class employs **State** and **Transition** Classes to calculate the intensities. The **State** takes into account how many muons it has, and the **Transitions** connected to **State** use the number of muons present in **State** to calculate how many muons flow through **Transition** to other connected **States** of lower energies. Each **Transition** considers how many muons that flow through it and therefore the intensity. This is done in a top to bottom approach starting from higher energy **States** to lower energy **States**. The **Sorter** Class is then used to sort results according to a particular way, in the current version of software the result is sorted with the greatest intensity displayed first.

There is a **NeuralNetwork** class that is used in classes which need to read from input files e.g., **IntensityCalculator** and **EnergyLevelTransitionMatrix**. This class was added later when it was noticed that there were NaN values present for some of the transition rates in the input file, this occurred in some very energetic transitions. These NaN values are introduced by the original Mudirac software when dividing by very small numbers. This value needed to be interpolated and the exact relation to predict the rates was not known so a neural network was used. The **NeuralNetwork** class creates a neural network to predict NaN values, a simple Multiple level perceptron with 20 hidden layers. This network was created using the **MLPRegressor** class in the Sci-kit learn python package. The input parameters that were used to train the neural network are shown below in the form of a 5-d vector:

$$[n1, \quad l1, \quad n2, \quad l2, \quad energy]$$

With a transition:

$$state1 \rightarrow state2$$

Where  $n1$  and  $l1$  are the energy level and total angular momentum numbers of state1 and  $n2$  and  $l2$  are the energy level and total angular momentum numbers associated with state2 and the energy is the energy of x-ray emitted from transition.

Figure 14 shows the effect of changing the size of the hidden layer, by increasing the size of the hidden layer the complexity of the network is increased. At lower complexities, the network performs poorly due to underfitting as the network is not complex enough to describe data well. While at high network complexities over-fitting occurs as the network describes training data too well and cannot be used to predict any dataset that is different from given training data [63] which is not shown in figure 14. With higher complexities comes higher training times so the chosen size of each hidden layer was 10, to get a balance between good performance and low training times. The method here used to characterize the performance of the network is the coefficient of determination  $R^2$  method with 1 being the best possible performance and the  $R^2$  value can be negative.



$$R^2 = 1 - \frac{\sum(y_{test} - y_{predicted})^2}{\sum(y_{test} - y_{test\_mean})^2} \quad (15)$$

Where  $y_{test}$  is the output of testing data set and  $y_{predicted}$  is the output predicted by the network and  $y_{test\_mean}$  is the mean of  $y_{test}$ .

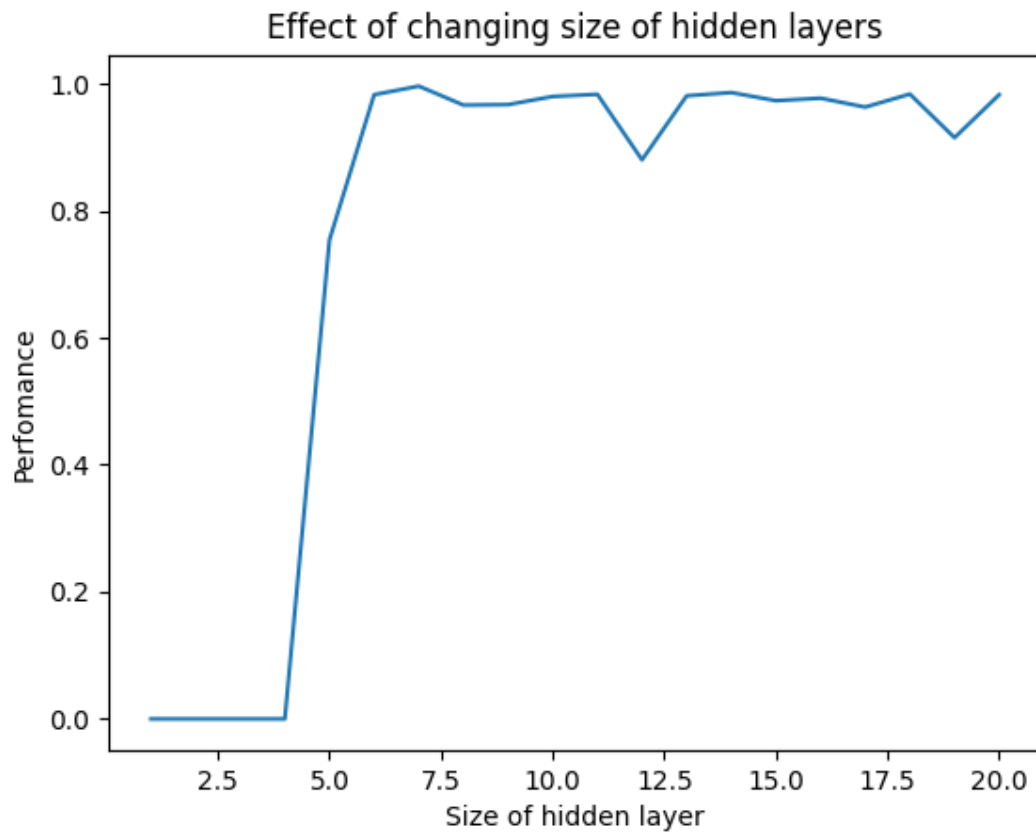


Figure 14: Graph showing the effect of changing the size of hidden layer on performance, evidence of underfitting is shown at lower levels.

# Experimental data from ISIS Neutron and Muon Source

To properly characterize the performance of software extension, it must be compared to experimental data, and so this data was collected at the ISIS Neutron and Muon source. This data was analysed using MANTID[64], a multiplatform open-source software framework that is used to analyse data from neutron and muon experiments.

## Production of muons at ISIS

ISIS is a pulsed source that is made up of 3 accelerators: a radio frequency quadrupole RFQ, a linear accelerator and a synchrotron.  $H^-$  ions are produced using a caesium-hydrogen plasma. These  $H^-$  ions are accelerated by the RFQ to 665 KeV, they are then transported to the linear accelerator where they are accelerated to 70 MeV. These  $H^-$  ions are then injected into the synchrotron every 20 milliseconds where they pass through a 0.3 micrometer thick carbon foil. This foil removes 2 electrons from the  $H^-$  ion making it a proton. This proton is then accelerated to 800 MeV by the synchrotron (which is about 84% the speed of light).

About 6% of the proton beam is diverted towards a graphite target in the Riken-RAL beamline, this interaction produces positive and negative pions in roughly equal amounts, these positive and negative pions decay with a half-life of 26 ns into positive and negative muons, respectively. Negative muons are diverted by magnets to Port 4 where the momentum of the muon can be controlled ranging from 17 MeV/c to 120 MeV/c with roughly a 2% spread in momentum [65].

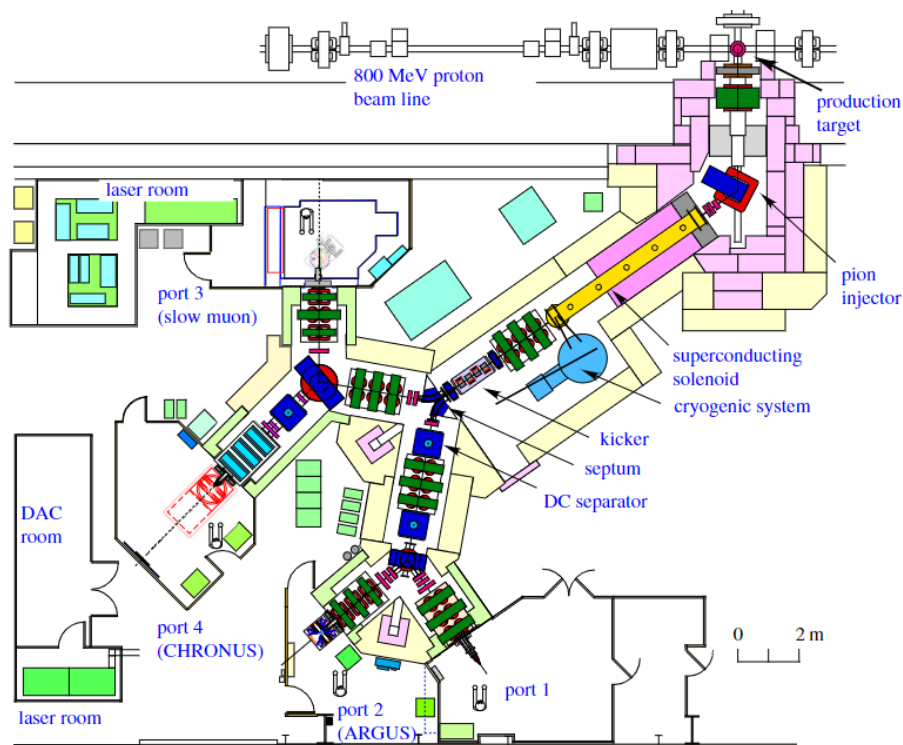


Figure 15: Diagram of Riken-RAL facility at ISIS Neutron and Muon source [65]

## Experimental setup and method

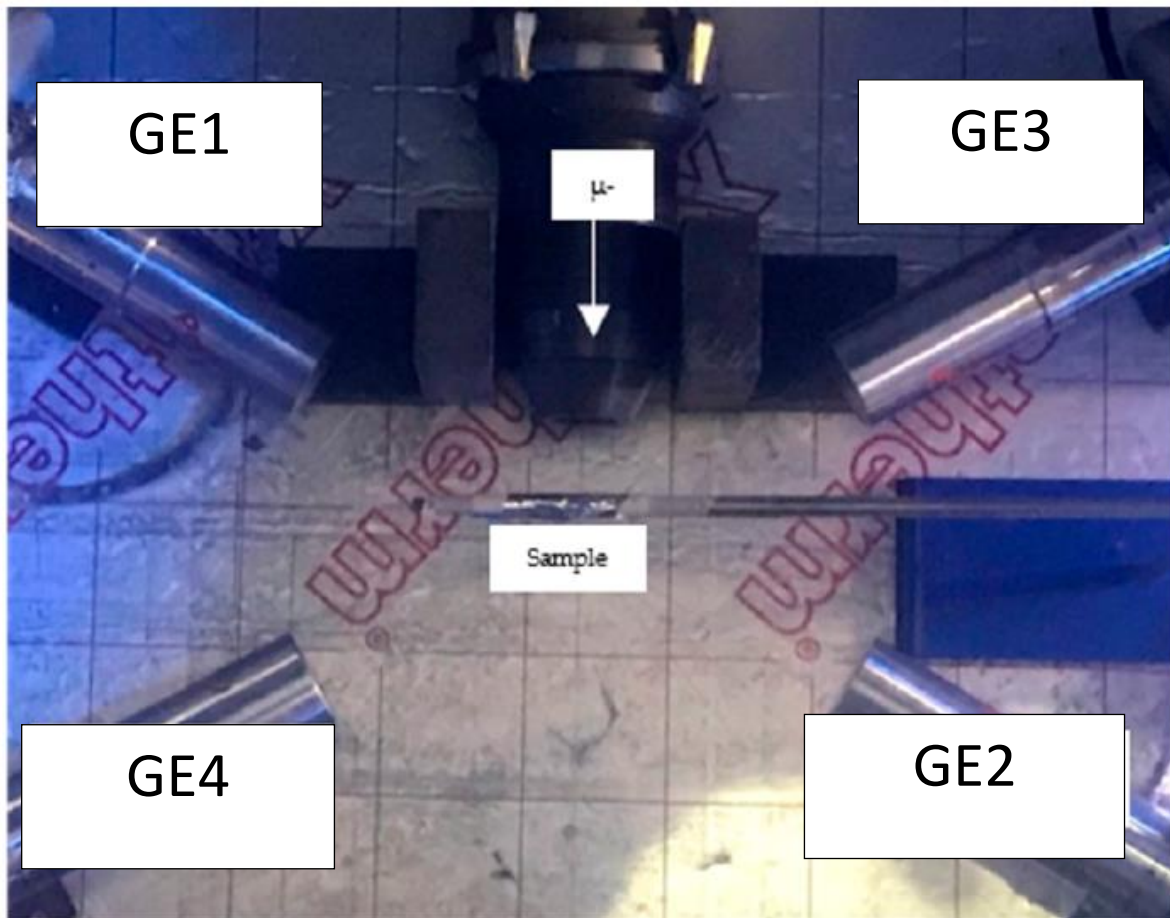


Figure 16: Image of the experimental setup

An image of the experimental setup at the ISIS Neutron and Muon source is given above. This setup utilizes 4 high purity germanium detectors:

- GE1: An Ortec GMX20P4, an n-type high energy detector ranging from about 100 KeV to 8 MeV, with a beryllium endcap.
- GE2: An Ortec GEM20P4-70-PL, a p-type high energy detector ranging from about 100 KeV to 8 MeV, with an aluminium endcap.
- GE3: An Ortec GEM-S5020P4-B, a p-type low energy detector ranging from about 50 KeV to 1 MeV, with a beryllium endcap.
- GE4: An Ortec GEM-S5020P4-B, a p-type low energy detector ranging from about 50 KeV to 1 MeV, with a beryllium endcap.

GE1 and GE3 are upstream detectors and so they suffer from much lower self-absorption effect than GE2 and GE4, So data from GE1 and GE3 were mostly used, Compared to GE1, GE3 has much lower efficiencies which led to higher count rates and lower error in data from GE1 but GE3 has much higher energy resolution and many peaks that could not be distinguished in GE1 could be distinguished in GE3 and so peaks that were close together

had to be analysed in GE3. Due to the higher resolution in GE3 data from GE3 was mostly used.

Detectors must be cooled to 77 kelvin using liquid nitrogen to reduce the noise caused by thermal energy at room temperature as the bandgap of germanium is small, otherwise, the noise would cause the detectors to be inoperable. Samples were placed in an Aluminum packet that is 0.016 mm thick and placed in front of the beam snout to be irradiated by muons.

## Analysis of Data

The samples were irradiated with muons with a momentum of 30 MeV/c the position of muons in the sample is of importance to know the layer under investigation and to calculate the self-absorption effect of the sample and the depth profile can be calculated using the software package SRIM treating the muon as a lighter negative hydrogen ion. This simulation is based on the Bethe-Bloch equation as this happens during the high energy slow-down phase of the muon. The depth and spread of muons in the samples as calculated by SRIM software considering the 2% spread of momentum is shown below in the table for each element analysed.

Element	Mean depth (mm)	Spread (mm)
Gold	0.155	0.030
Carbon	0.707	0.104
Copper	0.249	0.040
Silver	0.240	0.040
Lead	0.268	0.046
Silicon	0.780	0.118

Table 1: Table of depth and spread of muons in samples calculated by SRIM.

The self-absorption effect of the sample is not constant across all energies and was more prominent in lower energies, so was calculated using the depth profile of muons in the sample by finding the path of emitted x-rays to the detectors and calculating the length of the path  $d$  spent in the sample which also depends on factors like the geometry of sample and detector position. From the length of path  $d$  self-absorption for a particular energy can be calculated using the equation below.

$$I = e^{-\alpha d} \quad (16)$$

Where  $I$  is the relative intensity of x-rays reaching the detector compared to emitted intensities,  $\alpha$  is the element and energy-dependent absorption coefficient.

Another correction that was of importance was the fact that the efficiency of detectors had large variations within the area of interest, with the graph of efficiency against the energy of

detector 3 given below, with the efficiency of the other detectors following a similar shape.

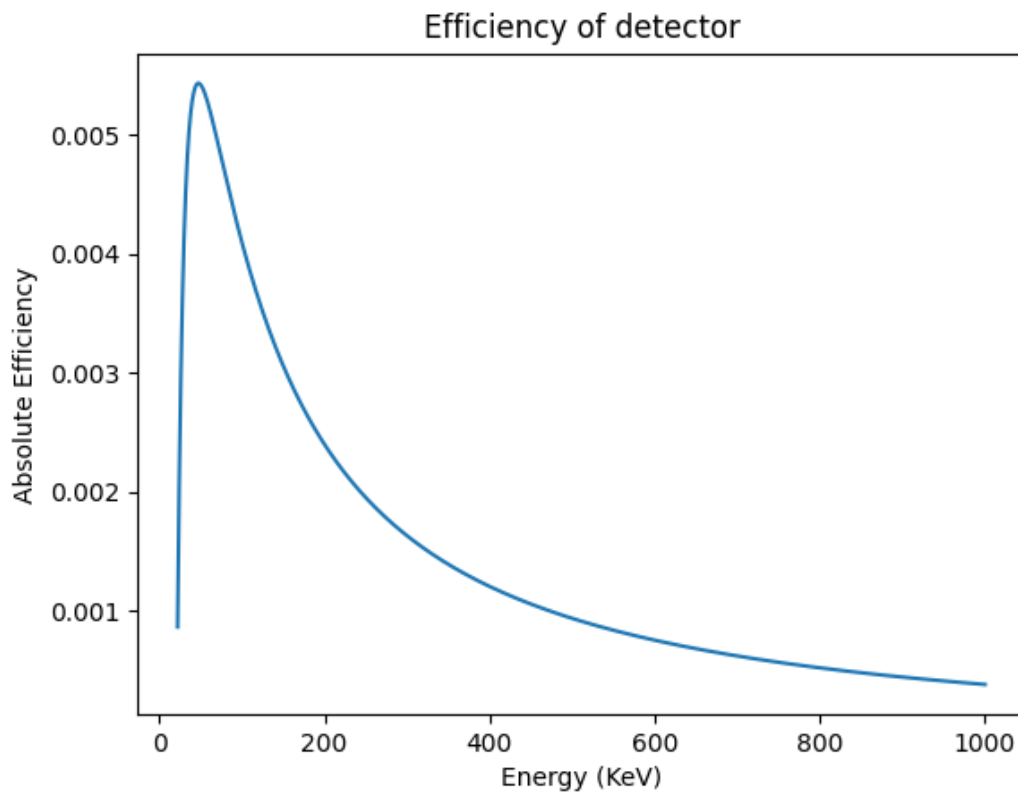


Figure 17: Graph of efficiency of detector 3

There were some issues in the energy calibration of detectors when analyzing data for some elements such as Ag, this was easily solved by using electron-positron annihilation peak at 511 KeV as a known calibration point.

The raw data and corrected data are shown below to show effects of corrections. As can be seen correction makes the peaks at lower energies smaller but the peaks at higher energies larger.

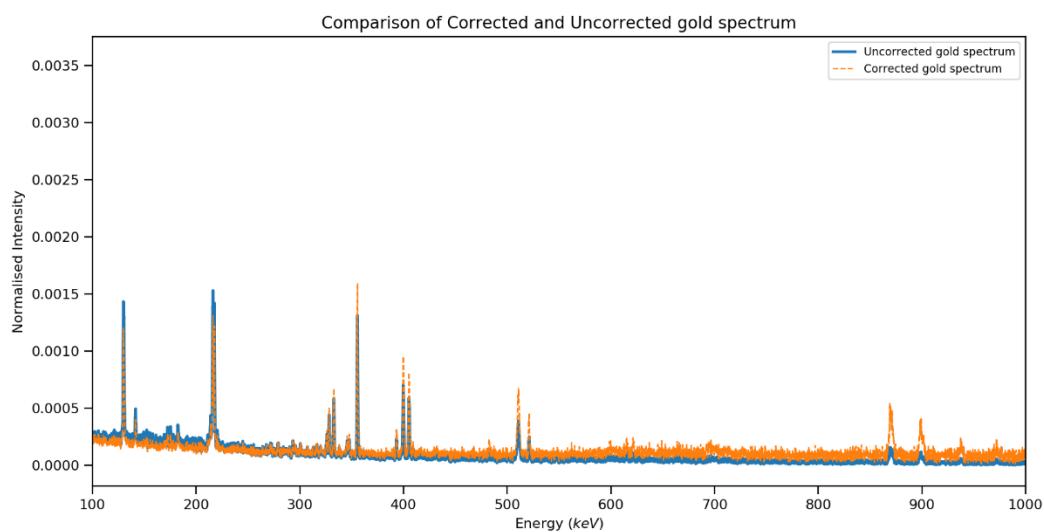


Figure 18: Graph of the corrected and uncorrected gold spectrum to show the effect of corrections

After all the corrections were applied, peaks in figure 18 with corrected data were modelled as gaussian and so are fitted to modified gaussian shown below in equation 17 with a linear background with the area of the peak being A. The minimizer that was used was the Levenburg-marquadt[60] algorithm using the least-squares cost function.

$$f(x) = \frac{A}{\sigma\sqrt{2\pi}} e^{-\frac{(x-x_0)^2}{\sigma^2}} + mx + c \quad (17)$$

$x_0$  is the peak center and  $\sigma$  is the standard deviation of gaussian with m and c being parameters for the linear background. The linear background was used to approximately model the background within the range of fit.

Some peaks were present in the spectrum that were not muonic x-rays these peaks are caused by gamma rays emitted from the nucleus. These peaks were ignored as they are not the objective of this project.

## Performance of software extension

The calculated and experimental intensities were used to create a bar chart, the bar charts show the results from major peaks present with the blue bar being the experimental data and the other colors corresponding the calculated intensities using a different I-distribution form. The transitions shown below are given using the IUPAC x-ray spectroscopy nomenclature [53]. It was noticed that lighter elements tended to have fewer peaks to analyse, as the energy of the majority of muonic x-rays they emit are smaller than the measurable 50 KeV limit.

### Carbon

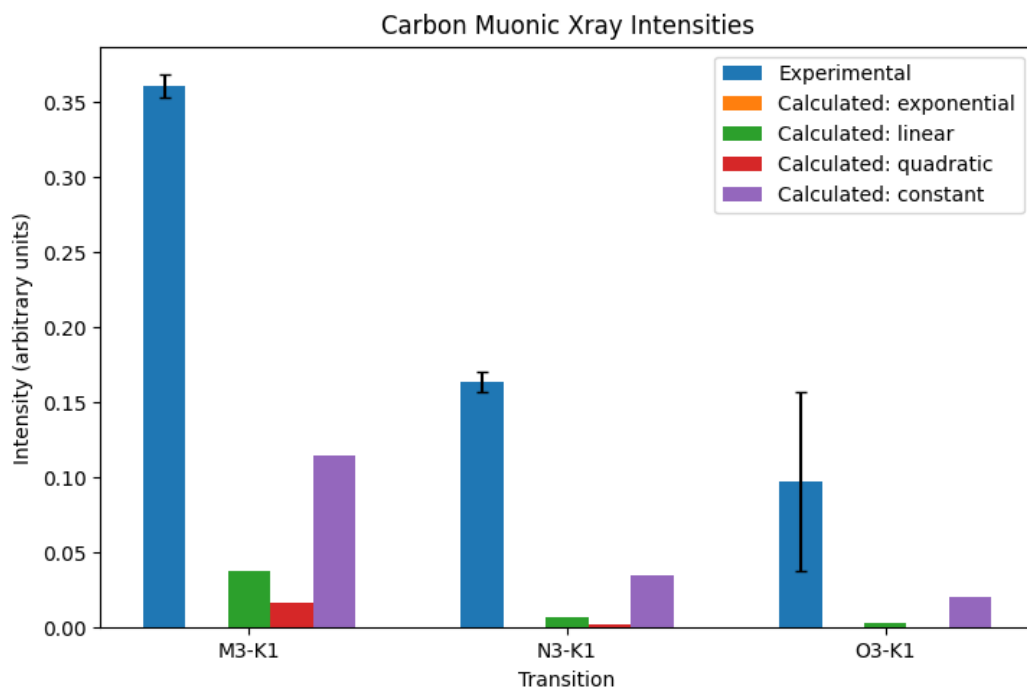


Figure 19: Graph of experimental and calculated muonic x-ray intensities from carbon.

## Silicon

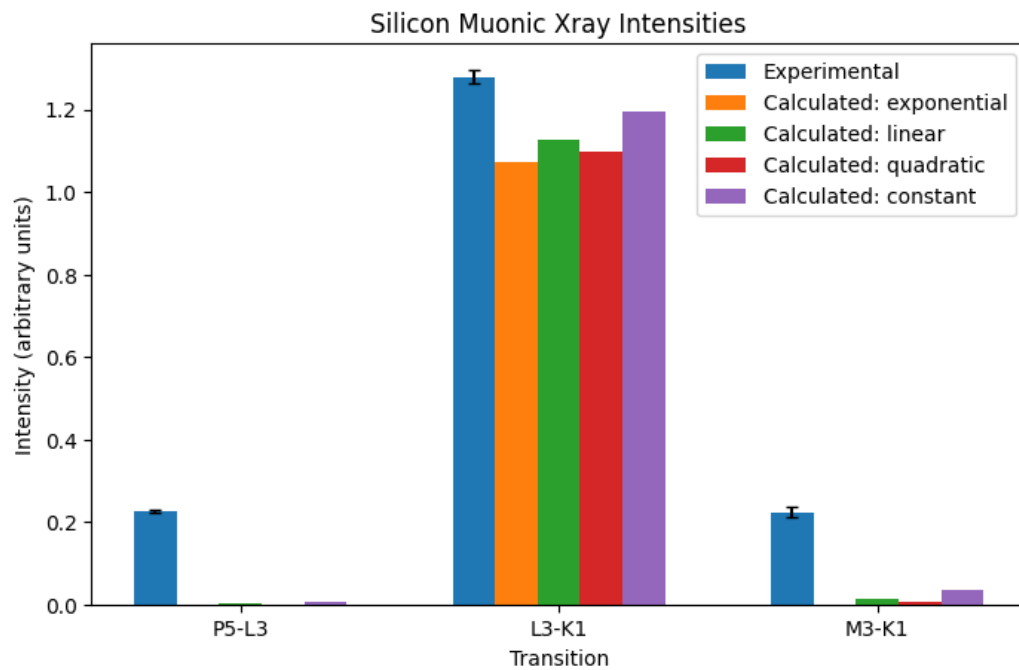


Figure 20: Graph of experimental and calculated muonic x-ray intensities from silicon.

## Copper

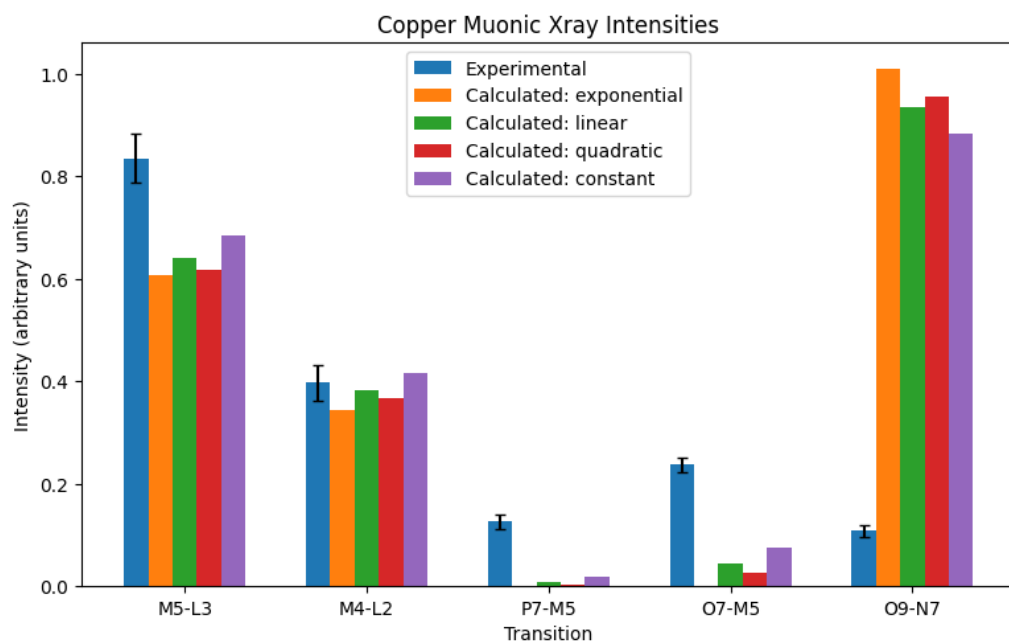


Figure 21: Graph of experimental and calculated muonic x-ray intensities from copper.



## Silver

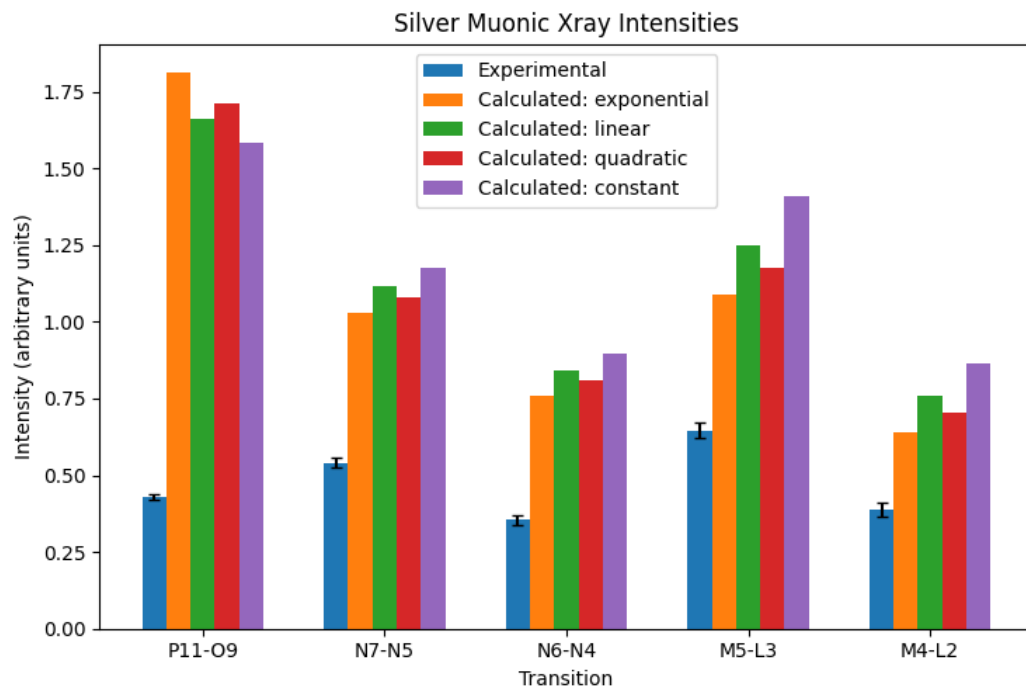


Figure 22: Graph of experimental and calculated muonic x-ray intensities from silver.

## Gold

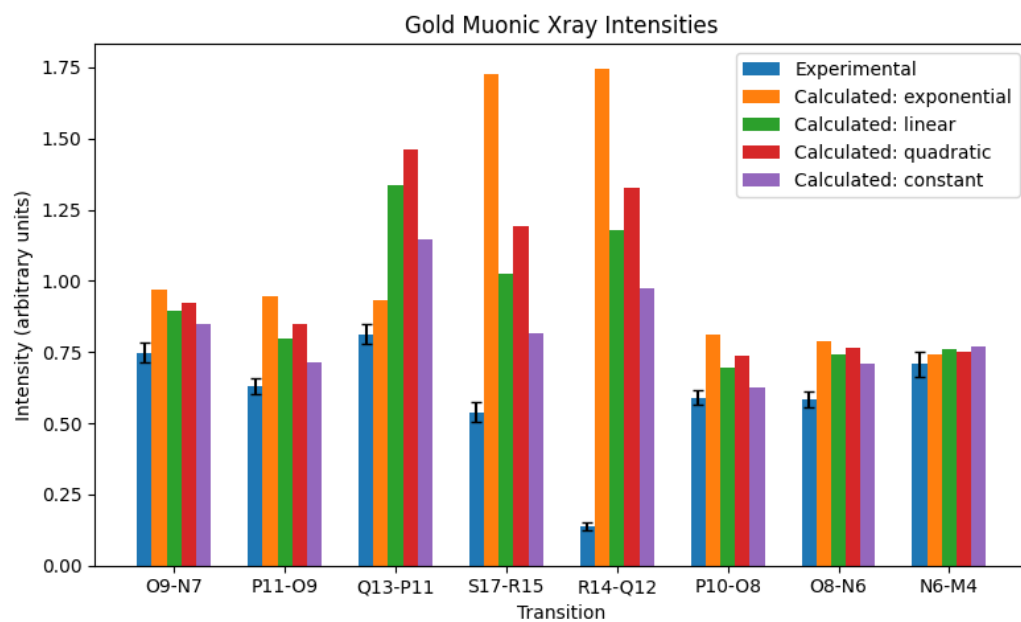


Figure 23: Graph of experimental and calculated muonic x-ray intensities from gold.

## Lead

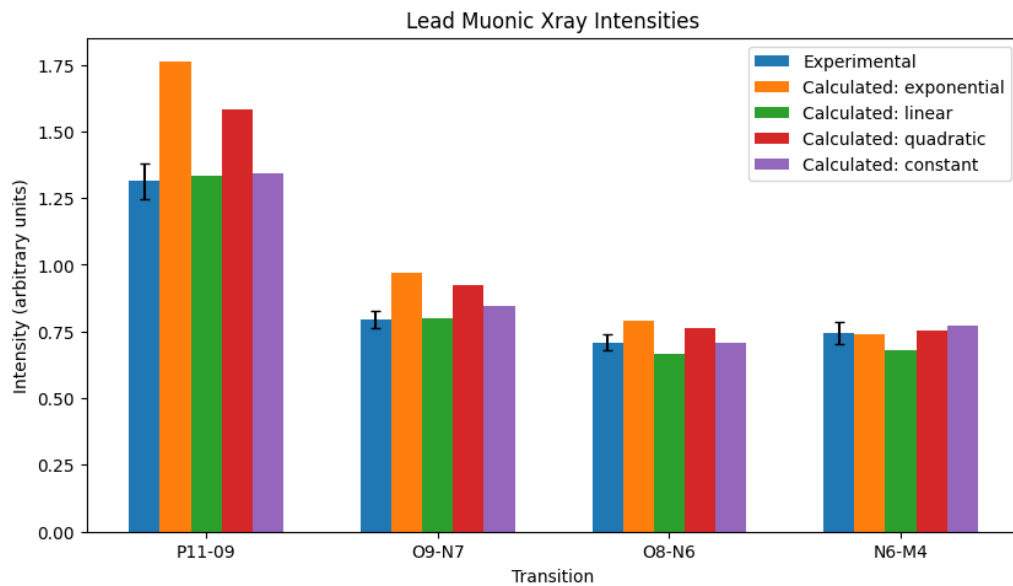


Figure 24: Graph of experimental and calculated muonic x-ray intensities from lead.

## Overview of bar charts

The table below summarizes results from bar charts, it gives the mean percentage differences between calculated intensities and experimental intensities.

Element	Exponential	Quadratic	Linear	Constant
Carbon	35726372.12	7410.49	1918.71	318.43
Silicon	224902010.71	10941.49	3477.87	1266.18
Copper	344256.60	752.42	362.13	173.45
Silver	51.43	54.25	56.14	59.37
Gold	35.90	35.34	31.88	25.40
Lead	13.49	9.68	4.56	2.95

Table 2: Table of percentage differences between calculated and experimental intensities for each of the l-distribution form.

## Use in elemental analysis

The spectrum from a bronze standard with a known composition was determined at ISIS Neutron and Muon sources, the composition is given below in table 3, standard has about 0.49 % of elements such as lead and arsenic, but these were ignored as there were no measurable peaks from these elements.

Element	Percentage
Copper	82.65 ± 0.51
Zinc	14.8 ± 0.05
Tin	2.06 ± 0.07

Table 3: Composition of bronze standard

The spectrum was analysed using the calculated intensities for each of the l-distribution forms with one peak corresponding to each element selected. For copper and zinc the N7-

N5 transition was chosen for Tin the O9-N7 transition was chosen. The calculated composition using calculated intensities are shown in table 4 below. The errors in composition come from measurement of peaks which were the same regardless of the I-distribution used.

L-distribution forms	Copper	Zinc	Tin
Constant	$80.71 \pm 0.73$	$14.29 \pm 0.41$	$4.99 \pm 0.40$
Linear	$80.94 \pm 0.73$	$14.33 \pm 0.41$	$4.73 \pm 0.37$
Exponential	$81.24 \pm 0.73$	$14.37 \pm 0.41$	$4.39 \pm 0.35$
Quadratic	$81.07 \pm 0.73$	$14.35 \pm 0.41$	$4.57 \pm 0.36$

Table 4: Calculated composition of bronze standard using different I-distribution forms.

## Discussion

As can be seen in table 2, the calculated intensities become more accurate as the nuclear mass increases. The I-distribution form that worked best was the constant form and the exponential form had the worst performance.

Although the software extension does not work well for many elements, the results do give some information on muon capture.

It can be inferred that the assumption of using the steady-state as the I-distribution was inaccurate and so therefore the I-distribution was not conserved when cascading in higher energy levels, as the exponential form which was the form that more closely resembled the calculated steady-state consistently had the worst performance as if it had been a good approximation the exponential would have the best performance.

From the results we can also infer that heavier elements capture muons at higher energy levels, As cascade stage was started at a high energy level which performed better in more massive atoms and worse for lower mass atoms as it is assumed that used starting energy level gets farther away from actual starting energy level the lighter the atom becomes. Heavier elements capture muons at higher energy levels due to their larger electronic orbital interacting with muons further out from the nuclei and so muon is captured further out at higher energy levels.

These results tell us that the software cannot be used for elements lighter than lead as calculated intensities for these lighter elements are very inaccurate.

It may be surprising to see that when the calculated intensities were used in the elemental analysis it produced relatively accurate results, which at first glance does not agree with initial assessment that calculated intensities are inaccurate for lighter elements, but during the elemental analysis it was noticed that while the intensities were inaccurate they were inflated by similar amounts so the ratio between these calculated intensities for between elements seem to reflect the real ratio but absolute value is inaccurate. The cause for this is unknown.

## Conclusion

The software extension might not perform as expected as the aim of the software was to calculate intensities for all elements reliably and can only be used to calculate intensities for elements heavier than lead. Many of the elements with nuclei more massive than lead are radioactive and so will not generally be used for muonic atom x-ray spectroscopy, and so the software will not have a practical use for those elements.

The shortcomings of software extension give valuable information for the next iteration of the software. Using this information from this project, the software can be improved by:

- Calculating the I-distribution ab initio using the system of integro-differential equations given in Appendix B.
- Studying low energy slow-down in-depth to better understand the effect of atomic mass on capture shells.
- Considering the possibility of muons being captured across more than one energy shell.
- Optimizing original Mudirac software to improve computation times by using threads.
- Improving electronic background calculation in Mudirac software by using DFT models for more accurate transition rates and x-ray energies.
- Studying cause of ratio of intensities reflecting actual intensities but not the absolute intensities.

## Acknowledgements

I would like to thank Dr Adrian Hillier for the experimental data from ISIS Neutron and Muon source at STFC, Dr Simone Sturniolo from the Scientific Computing Department at STFC for discussions on how software extension should work, Dr Alun Jones for assistance with computing resources and Dr Dave Langstaff for his supervision during the project.

## Appendix A

There were 5 different I-distributions highlighted by Hartmann et al[21] and are given below:

1.  $N_{init}(l) \propto 2l + 1$  (18)

This distribution means that the probability of being populated depends on the number of states present.

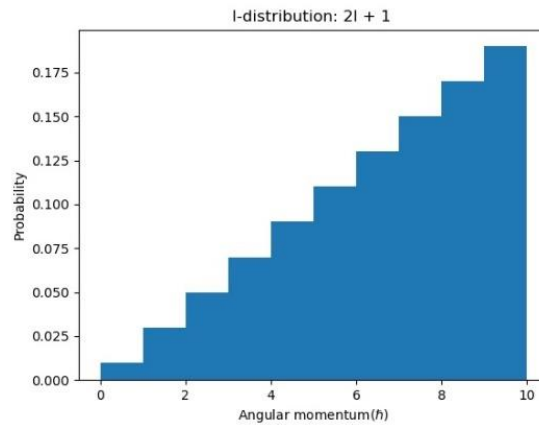


Figure 25: Graph of I-distribution form: 2l+1

2.  $N_{init}(l) \propto (2l + 1)e^{al}$  (19)

This distribution gives precedence to states with higher angular momenta, this form was also used by Eisenberg and Kessler with a being 0.2[22].

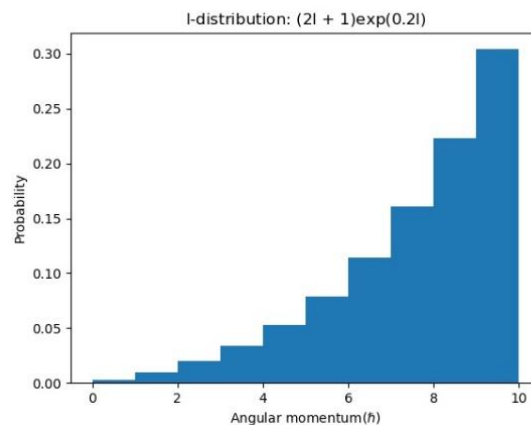


Figure 26: Graph of I-distribution form:  $(2l + 1)e^{al}$

3.  $N_{init}(l) \propto \text{constant}$  (20)

This distribution means that all states are equally probable to be occupied.

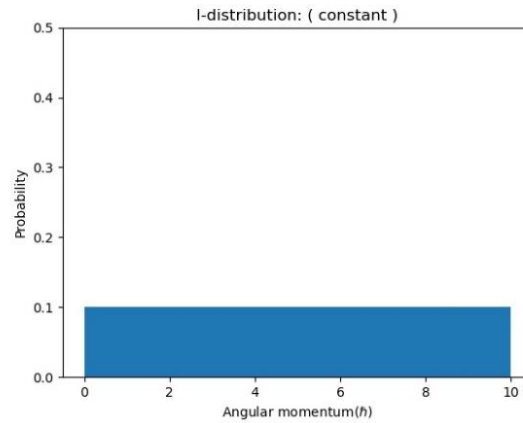


Figure 27: Graph of I-distribution form which is a constant

$$4. \quad N_{init}(l) \propto l \quad (21)$$

This distribution is like the first distribution, but the only difference is the first state.

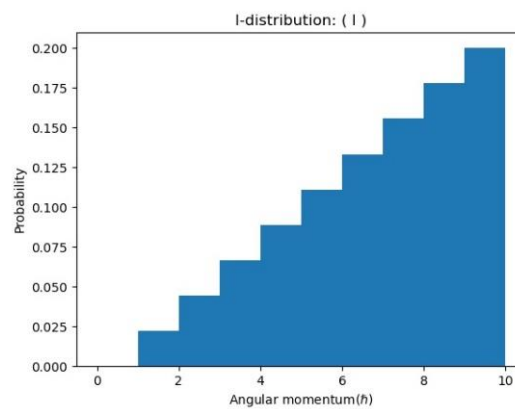


Figure 28: Graph of I-distribution form: l

$$5. \quad N_{init}(l) \propto 1 + al \quad (22)$$

This distribution is similar to the first distribution, but the only difference is the first state

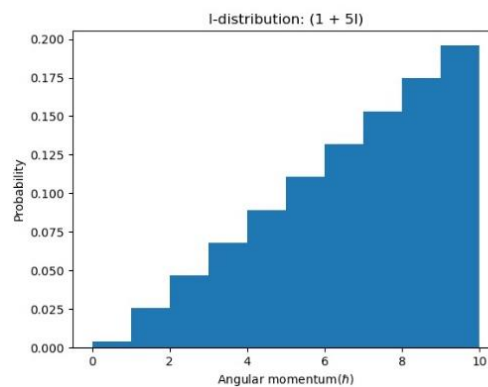


Figure 29: Graph of I-distribution form: 1 + al

The l-distribution form used by Vogel is given below where  $n$  is the energy level of interest and is a parameter in the form, unlike the other forms where it only depended on angular momentum [23].

$$N_{init}(l) = \frac{1}{n} + b \left[ l - \frac{1}{2}(n-1) \right] + c \left[ l^2 - \frac{1}{6}(n-1)(2n-1) \right] \quad (23)$$

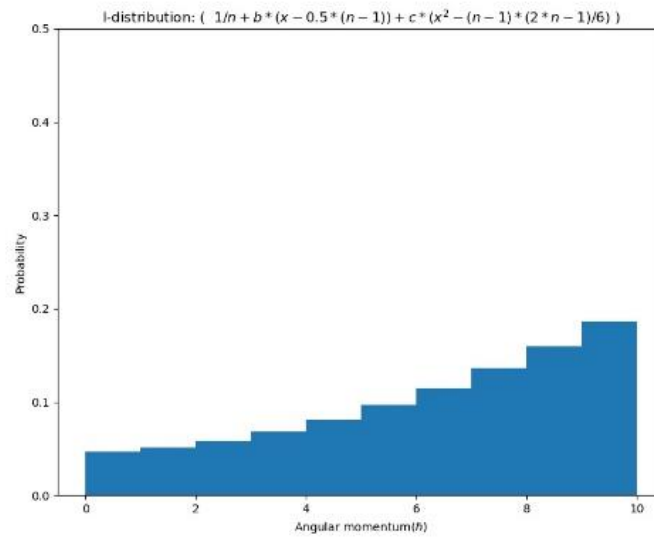


Figure 30: Graph showing l-distribution suggested by Vogel [23]



## Appendix B

The I-distribution of muons can be calculated using the probability that the muon will have lost energy  $\epsilon$  at time  $t$   $\frac{dP_t(\epsilon)}{d\epsilon}$  using equation 2 [25].

$$\frac{d}{dt} \left( \frac{dP_t(\epsilon)}{d\epsilon} \right) = \int \left( \frac{dP_t(\epsilon - \delta)}{d\epsilon} - \frac{dP_t(\epsilon)}{d\epsilon} \right) \frac{d^2 p(\delta)}{d\delta dt} d\delta \quad (24)$$

But before being able to calculate the I-distribution the capture cross-section (the cross-section that a muon of energy  $E$  is captured) and the cross-section of a muon of energy  $E$  to lose energy  $\epsilon$  needs to be calculated [66] and are given below respectively.

$$\sigma_{cap}(E) = 2\pi \int_0^d b db \int_{E-E_{bar}(b)}^{\infty} \frac{dP_t(\epsilon)}{d\epsilon} d\epsilon \quad (25)$$

$$\frac{d\sigma_{\epsilon}(E)}{d\epsilon} = 2\pi \int_0^d \frac{dP_t(\epsilon < E - E_{bar}(b))}{d\epsilon} b db \quad (26)$$

Where  $b$  is the impact parameter,  $d$  is a quantity that represents the size of the atom,  $E_{bar}$  is the energy of the potential barrier

Both cross-sections are then used to calculate the probability per unit energy and area of a muon having an energy  $E$  not being captured ( $R$ ).

$$R(E) \left\{ \sigma_{cap}(E) + \int_0^E \frac{d\sigma_{\epsilon}(E)}{d\epsilon} d\epsilon \right\} = \int_0^{\infty} \frac{d\sigma_{\epsilon}(E+\epsilon)}{d\epsilon} R(E+\epsilon) d\epsilon \quad (27)$$

$R(E)$  is then used to calculate  $\Delta N(l)$  the number of muons captured with an angular momentum within  $\Delta l$

$$\Delta N(l) = \frac{h^2 l \Delta l \pi}{m} \int_0^{\infty} \frac{R(E)}{E} dE \int_{E-E_{bar}(l)}^{\infty} \frac{dP_t(\epsilon)}{d\epsilon} d\epsilon \quad (28)$$

These cross-sections are not just useful in calculating the I-distribution but also useful in calculating the capture ratios of muons in a compound which is not shown here.

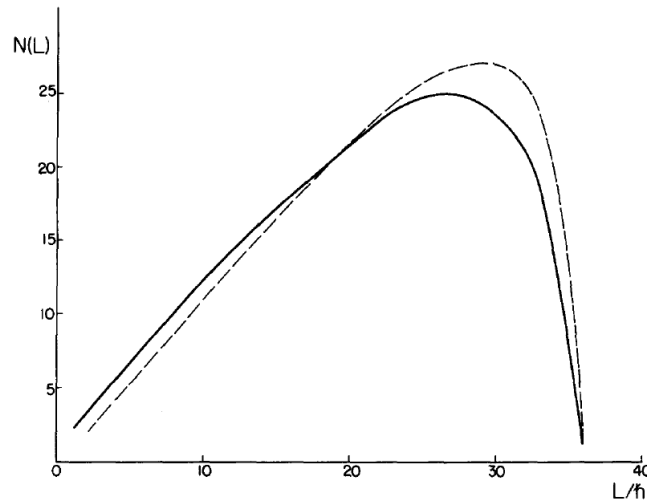


Figure 31: Graph showing I-distribution calculated using the method above, with the solid line being the I-distribution at the time of capture in a neutral argon atom and the dotted line being the I-distribution when the muon is at  $n = 11$  [26].

## Appendix C

When given a set of  $n$  independent variables  $x_1, x_2, \dots, x_n$  and a set of  $n$  dependent variables  $y_1, y_2, \dots, y_n$ . These variables can be fitted to a known function  $f(x)$  with  $m$  parameters to be fitted. Fitting works by finding the optimum set of  $m$  parameters  $p_1, p_2, \dots, p_m$  that results in the best fit of function to data. For a fit to be successful  $n$  must be greater than or equal to  $m$ . And an initial guess of parameters must be given to the fitting algorithm to start with.

To determine the optimum parameters there must be a cost function, which determines how a set of parameters perform. The simplest and most commonly used cost function is the least-squares cost function, which was used everywhere in this project where fitting was applicable and is shown below:

$$C(p_1, p_2, \dots, p_m) = \sum_i^n (y_i - f(x_i, p_1, p_2, \dots, p_m))^2 \quad (29)$$

While we may have a cost function, there must be an algorithm to quickly get to optimum parameters, which is called a minimizer. One such minimizer that is commonly used is the Levenburg-Marquardt minimizer, this minimizer is a mixture of the Gauss-Newton algorithm and the gradient descent, which is the simplest minimizer. Minimizers work by finding the solution to equation 30 below for all parameters as optimum parameters occurs at minimums of derivative of the cost function.

$$\frac{dC(p_1, p_2, \dots, p_n)}{dp_i} = 0 \quad (30)$$

## Bibliography

1. Measday, D.F., *The nuclear physics of muon capture*. Physics Reports, 2001. **354**(4-5): p. 243-409.
2. Weinberger, P., *All you need to know about the Dirac equation*. Philosophical Magazine, 2008. **88**(18-20): p. 2585-2601.
3. Sturniolo, S. and A. Hillier, *Mudirac: A Dirac equation solver for elemental analysis with muonic X-rays*. X-Ray Spectrometry, 2021. **50**(3): p. 180-196.
4. Mohr, P.J., et al., *The NIST Reference on Constants, Units, and Uncertainty*. 2018 CODATA, 2019.
5. Beringer, J., *PDG Live Particle Summary Quarks (u, d, s, c, b, t, b', t', Free)*. Particle Data Group, PR D86, 010001. 2012.
6. Eckhause, M., et al., *Measurements of Negative-Muon Lifetimes in Light Isotopes*. Physical Review, 1963. **132**(1): p. 422.
7. Martin, B.R. and G. Shaw, *Particle physics*. 2nd ed. Manchester physics series. 1997, Chichester: Wiley.
8. Mukhopadhyay, N.C., *Nuclear Muon capture*. Physics Reports, 1977. **30**(1): p. 1-144.
9. Bethe, H.A., *Penetration of fast charged particles through matter*. Ann. Physik, 1930. **5**: p. 325.
10. Bloch, F., *Bremsvermögen von Atomen mit mehreren Elektronen*. Zeitschrift für Physik, 1933. **81**(5): p. 363-376.
11. Ziegler, J.F., *Stopping of energetic light ions in elemental matter*. Journal of applied physics, 1999. **85**(3): p. 1249-1272.
12. Ahlen, S.P. and G. Tarlé, *Observation of large deviations from the Bethe-Bloch formula for relativistic uranium ions*. Physical Review Letters, 1983. **50**(15): p. 1110.
13. Groom, D.E. and S.R. Klein, *Passage of particles through matter*. The European Physical Journal C-Particles and Fields, 2000. **15**(1): p. 163-173.
14. Fermi, E. and E. Teller, *The Capture of Negative Mesotrons in Matter*. Physical Review, 1947. **72**(5): p. 399-408.
15. Lindhard, J. and A. Winther, *Stopping power of electron gas and equipartition rule*. 1964: Munksgaard.
16. Haff, P.K., P. Vogel, and A. Winther, *Capture of negative muons in atoms*. Physical Review A, 1974. **10**(4): p. 1430.
17. Lenz, W., *Über die Anwendbarkeit der statistischen Methode auf Ionengitter*. Zeitschrift für Physik, 1932. **77**(11-12): p. 713-721.
18. Von Egidy, T. and F.J. Hartmann, *Average muonic Coulomb capture probabilities for 65 elements*. Physical Review A, 1982. **26**(5): p. 2355.
19. Vogel, P., A. Winther, and V. Akylas, *On the capture of muons in atoms*. Physics Letters B, 1977. **70**(1): p. 39-42.
20. Akylas, V.R. and P. Vogel, *Muonic atom cascade program*. Computer Physics Communications, 1978. **15**(3-4): p. 291-302.
21. Hartmann, F.J., et al., *Measurement of the muonic x-ray cascade in Mg, Al, In, Ho, and Au*. Zeitschrift für Physik A Atoms and Nuclei, 1982. **305**(3): p. 189-204.
22. Eisenberg, Y. and D. Kessler, *On the  $\mu$ -mesonic atoms*. Il Nuovo Cimento (1955-1965), 1961. **19**(6): p. 1195-1210.
23. Vogel, P., *Muonic cascade: General discussion and application to the third-row elements*. Physical Review A, 1980. **22**(4): p. 1600.

24. Haff, P.K. and T.A. Tombrello, *Negative muon capture in very light atoms*. Annals of Physics, 1974. **86**(1): p. 178-192.
25. Akylas, V.R., *Cascade of Negative Muons in Atoms*. 1978, DTIE (Division of Technical Information Extension, US Atomic Energy Commission).
26. Vogel, P., et al., *Muon capture in atoms, crystals and molecules*. Nuclear Physics A, 1975. **254**(2): p. 445-479.
27. Markushin, V.E., *Cascade in muonic and pionic atoms with  $Z=1$* . Hyperfine interactions, 1999. **119**(1): p. 11-21.
28. Clemenza, M., et al., *Muonic atom x-ray spectroscopy for non-destructive analysis of archeological samples*. Journal of Radioanalytical and Nuclear Chemistry, 2019. **322**(3): p. 1357-1363.
29. Hartmann, F.J., et al., *Measurement of the muonic X-ray cascade in metallic iron*. Physical Review Letters, 1976. **37**(6): p. 331.
30. Green, G.A., et al., *Understanding Roman Gold Coinage Inside Out*. Journal of Archaeological Science, 2021. **134**: p. 105470.
31. Suzuki, T., D.F. Measday, and J.P. Roalsvig, *Total nuclear capture rates for negative muons*. Physical Review C, 1987. **35**(6): p. 2212.
32. Bardin, G., et al., *Total muon capture rate in  $^6\text{Li}$  and  $^7\text{Li}$* . Physics Letters B, 1978. **79**(1-2): p. 52-54.
33. Evans, H.J., *Gamma-rays following muon capture*. Nuclear Physics A, 1973. **207**(2): p. 379-400.
34. Budick, B., R. Anigstein, and J.W. Kast, *Delayed gamma rays from muon capture on  $^{207}\text{Pb}$* . Nuclear Physics A, 1983. **393**(3): p. 469-490.
35. Cazzaniga, C., et al., *Neutron activation analysis of archeological artifacts using the ISIS pulsed neutron source*. AIP Advances, 2021. **11**(7): p. 075005.
36. Phipps, C., *Laser ablation and its applications*. Vol. 129. 2007: Springer.
37. Hore, P.J., *Nuclear magnetic resonance*. 2015: Oxford University Press, USA.
38. Shackley, M.S., *An introduction to X-ray fluorescence (XRF) analysis in archaeology, in X-ray fluorescence spectrometry (XRF) in geoarchaeology*. 2011, Springer. p. 7-44.
39. Ninomiya, K., et al. *Development of elemental analysis by muonic X-ray measurement in J-PARC*. IOP Publishing.
40. Hillier, A.D., D.M. Paul, and K. Ishida, *Probing beneath the surface without a scratch—Bulk non-destructive elemental analysis using negative muons*. Microchemical Journal, 2016. **125**: p. 203-207.
41. Ziegler, J.F., M.D. Ziegler, and J.P. Biersack, *SRIM—The stopping and range of ions in matter (2010)*. Nuclear Instruments and Methods in Physics Research Section B: Beam Interactions with Materials and Atoms, 2010. **268**(11-12): p. 1818-1823.
42. Hutson, R.L., et al., *Tissue chemical analysis with muonic x rays*. Radiology, 1976. **120**(1): p. 193-198.
43. Umegaki, I., et al., *Nondestructive high-sensitivity detections of metallic lithium deposited on a battery anode using muonic X-rays*. Analytical Chemistry, 2020. **92**(12): p. 8194-8200.
44. Köhler, E., et al., *Application of muonic X-ray techniques to the elemental analysis of archeological objects*. Nuclear Instruments and Methods in Physics Research, 1981. **187**(2-3): p. 563-568.
45. Hampshire, B.V., et al., *Using negative muons as a probe for depth profiling silver roman coinage*. Heritage, 2019. **2**(1): p. 400-407.

46. Clemenza, M., et al., *CHNET-TANDEM experiment: Use of negative muons at RIKEN-RAL Port4 for elemental characterization of "Nuragic votive ship" samples*. Nuclear Instruments and Methods in Physics Research Section A: Accelerators, Spectrometers, Detectors and Associated Equipment, 2019. **936**: p. 27-28.
47. Terada, K., et al., *Non-destructive elemental analysis of a carbonaceous chondrite with direct current Muon beam at MuSIC*. Scientific reports, 2017. **7**(1): p. 1-6.
48. Brown, K.L., et al., *Depth dependant element analysis of PbMg<sub>1</sub>/3Nb<sub>2</sub>/3O<sub>3</sub> using muonic x-rays*. Journal of Physics: Condensed Matter, 2018. **30**(12): p. 125703.
49. Ninomiya, K., et al., *Development of non-destructive isotopic analysis methods using muon beams and their application to the analysis of lead*. Journal of Radioanalytical and Nuclear Chemistry, 2019. **320**(3): p. 801-805.
50. Aramini, M., et al., *Using the Emission of Muonic X-rays as a Spectroscopic Tool for the Investigation of the Local Chemistry of Elements*. Nanomaterials, 2020. **10**(7): p. 1260.
51. Hillier, A., et al. *Element specific imaging using muonic x-rays*.
52. Kudo, T., et al., *Development of a non-destructive isotopic analysis method by gamma-ray emission measurement after negative muon irradiation*. Journal of Radioanalytical and Nuclear Chemistry, 2019. **322**(3): p. 1299-1303.
53. Jenkins, R., et al., *IUPAC—nomenclature system for x-ray spectroscopy*. X-Ray Spectrometry, 1991. **20**(3): p. 149-155.
54. Silbar, R.R. and T. Goldman, *Solving the radial Dirac equations: a numerical odyssey*. European journal of physics, 2010. **32**(1): p. 217.
55. Müller, C., *Spherical harmonics*. Vol. 17. 2006: Springer.
56. Uehling, E.A., *Polarization effects in the positron theory*. Physical Review, 1935. **48**(1): p. 55.
57. Tauscher, L., et al., *Precision measurement of the muonic 5-4 transitions in Pb and 4-3 transitions in ba as a test for the validity of QED*. Zeitschrift für Physik A Atoms and Nuclei, 1978. **285**(2): p. 139-158.
58. Chivers, I. and J. Sleightholme, *An introduction to Algorithms and the Big O Notation*, in *Introduction to programming with Fortran*. 2015, Springer. p. 359-364.
59. Hamoud, A.A., et al., *Solving integro-differential equations by using numerical techniques*. International Journal of Applied Engineering Research, 2019. **14**(14): p. 3219-3225.
60. Moré, J.J., *The Levenberg-Marquardt algorithm: implementation and theory*, in *Numerical analysis*. 1978, Springer. p. 105-116.
61. Lutz, M., *Programming python*. 2001: " O'Reilly Media, Inc."
62. VanderPlas, J., *Python data science handbook: Essential tools for working with data*. 2016: " O'Reilly Media, Inc."
63. Marsland, S., *Machine learning: an algorithmic perspective*. 2011: Chapman and Hall/CRC.
64. Arnold, O., et al., *Mantid—Data analysis and visualization package for neutron scattering and  $\mu$  SR experiments*. Nuclear Instruments and Methods in Physics Research Section A: Accelerators, Spectrometers, Detectors and Associated Equipment, 2014. **764**: p. 156-166.
65. Hillier, A.D., et al., *Muons at ISIS*. Philosophical Transactions of the Royal Society A, 2019. **377**(2137): p. 20180064.

66. Vogel, P., *Capture of muons in atoms.[Lecture, atomic cascade]*. 1978, California Inst. of Tech., Pasadena (USA).